Draft version June 6, 2018
Preprint typeset using LaTeX style emulateapj v. 12/16/11

THE LYMAN CONTINUUM ESCAPE SURVEY: IONIZING RADIATION FROM [O III]-STRONG SOURCES AT A REDSHIFT OF 3.1

Thomas J. Fletcher[1], Brant E. Robertson[2], Kimihiko Nakajima[1,3,4], Richard S. Ellis[1], Daniel P. Stark[5], Akio Inoue[6]

Draft version June 6, 2018

ABSTRACT

We present results from the LymAn Continuum Escape Survey (LACES), a Hubble Space Telescope (HST) program designed to characterize the ionizing radiation emerging from a sample of Lyman alpha emitting galaxies at redshift $z \simeq 3.1$. As many show intense [O III] emission characteristic of $z > 6.5$ star-forming galaxies, they may represent valuable low redshift analogs of galaxies in the reionization era. Using HST Wide Field Camera 3 / UVIS $F336W$ to image Lyman continuum emission, we investigate the escape fraction of ionizing photons in this sample. For 61 sources, of which 77% are spectroscopically confirmed and 53 have measures of [O III] emission, we detect Lyman continuum leakage in 30%, a rate significantly higher than in continuum-selected Lyman break galaxies. We estimate there is a 97% probability that ≤ 3 of our detections could be affected by foreground contamination. Fitting multi-band spectral energy distributions (SEDs) to take account of the varying stellar populations, dust extinctions and metallicities, we derive individual Lyman continuum escape fractions corrected for foreground intergalactic absorption. We find escape fractions of 2 to 82% for individual objects, and infer an average 20% escape fraction by fitting composite SEDs for our detected samples. Surprisingly however, even a deep stack of those sources with no individual $F336W$ detections provides a stringent upper limit on the average escape fraction of less than 0.3%. We examine various correlations with source properties and discuss the implications in the context of the popular picture that cosmic reionization is driven by such compact, low metallicity star-forming galaxies.

Subject headings: galaxies: distances and redshifts, evolution, formation, star formation – cosmology : early universe – infrared: galaxies

1. INTRODUCTION

Deep imaging with the WFC3/IR camera on-board HST has dramatically expanded our redshift horizon, making it practical to address two long-standing cosmological questions: (i) when did the Universe transition from a neutral to an ionized state, and (ii) were early star-forming galaxies responsible for this cosmic reionization? Multi-color HST/Spitzer imaging in the Ultra Deep Field (UDF; Beckwith et al. 2006; Ellis et al. 2013; Koekemoer et al. 2013; Illingworth et al. 2013) and the CANDELS fields (Grogin et al. 2011; Koekemoer et al. 2011; Oesch et al. 2013; Bouwens et al. 2015), together with complementary studies undertaken through the CLASH (Bradley et al. 2014) and Frontier Field (McLeod et al. 2015; Lotz et al. 2017) lensing clusters, have delivered several hundred $z > 7$ Lyman break galaxy (LBG) candidates providing the first convincing description of the abundance and luminosity distribution (McLure et al. 2013; Atek et al. 2015; Finkelstein et al. 2015; Bouwens et al. 2015; Livermore et al. 2017; Ishigaki et al. 2018) of early star-forming galaxies to $z \simeq 10$ (see Stark 2016 for a review).

The optical depth, τ, of electron scattering to the cosmic microwave background measured by the Planck consortium (Planck 2015) constrains the redshift window over which reionization occurred. Robertson et al. (2015) demonstrated how the demographics of star-forming galaxies determined by HST can be reconciled with this value in terms of a reionization history over the redshift range $6 \lesssim z \lesssim 12$ given some significant assumptions about the ionizing capability of the typical, most abundant, low luminosity sources. The key assumptions relate to (i) the UV radiation emerging from their stellar populations, defined by Robertson et al. (2013) in terms of $\xi_{\rm ion}$, the number of Lyman continuum (LyC) photons produced per UV (1500 Å) luminosity, and (ii) the fraction $f_{\rm esc}$ of such LyC photons that can escape absorption within the galaxy and its immediate vicinity. The quantity $\xi_{\rm ion}$ cannot be determined from broad-band photometry alone (Robertson et al. 2013) and is best constrained from Balmer line emission using recombination physics with a weak dependence on $f_{\rm esc}$ (Bouwens et al. 2016). Until JWST is launched, the relevant lines are beyond reach of ground-based spectrographs at high redshift. Likewise the opacity of the intergalactic medium at UV wavelengths becomes too great beyond $z \simeq 4$ to determine $f_{\rm esc}$ from deep HST imaging below the Lyman limit (e.g., Shapley et al. 2006). Therefore, neither of these quantities can be constrained for galaxies in the

[1] Department of Physics and Astronomy, University College London, Gower Street, London WC1E 6BT, UK
[2] Department of Astronomy & Astrophysics, University of California, Santa Cruz, 1156 High St, Santa Cruz CA 95064, USA
[3] European Southern Observatory (ESO), Karl-Schwarzschild-Strasse 2, 85748 Garching, Germany
[4] National Astronomical Observatory of Japan, 2-21-1 Osawa, Mitaka, Tokyo 181-8588, Japan
[5] Steward Observatory, University of Arizona, 933 N Cherry Ave, Tucson, AZ 85721, USA
[6] Osaka Sangyo University, 3-1-1 Nakagaito, Daito, Osaka 574-8530 Japan

reionization era with current facilities, yet they collectively comprise the primary uncertainty in claims that reionization is driven by star-forming galaxies. The situation is particularly critical for $f_{\rm esc}$ since Robertson et al. (2013, 2015) argued a mean value of $10-20\%$ is required for galaxies to reionize the Universe, whereas studies at redshifts where LyC photons can be directly detected frequently yield upper limits of $f_{esc} \lesssim 5\%$ (e.g., Siana et al. 2015; Mostardi et al. 2015)

In promoting the view that early star-forming galaxies reionized the Universe, many workers have speculated that the both the intensity of the ionizing radiation (effectively $\xi_{\rm ion}$) and the porosity of neutral gas in the circumgalactic medium (i.e. $f_{\rm esc}$) increase with redshift, particularly for compact, intensely star-forming systems (Inoue et al. 2006; Kuhlen & Faucher-Giguère 2012; Robertson et al. 2013; Finkelstein et al. 2015). Indeed, the strength of nebular emission (e.g., [O III] 5007 Å), whether measured directly from near-infrared spectroscopy (Schenker et al. 2013), or inferred indirectly from the excess flux in Spitzer photometry (Labbé et al. 2013; Smit et al. 2014, 2015), does apparently increase with redshift. Surprisingly, some of the most luminous LBGs with large $\rm EW_{[O\,III]}$ at $z > 7$ (Roberts-Borsani et al. 2016) also reveal Lyα in emission (Oesch et al. 2015; Zitrin et al. 2015; Laporte et al. 2017; Stark et al. 2017), 'bucking the trend' established for less luminous systems. This correlation may imply that sources with large $\rm EW_{[O\,III]}$ also have a high value of $f_{\rm esc}$, thereby creating early ionized bubbles that permit Lyα photons to emerge (Stark et al. 2017).

The inter-dependence of large $\rm EW_{[O\,III]}$, a higher than average value of $\xi_{\rm ion}$, and the leakage of LyC photons was first evaluated in the context of photoionization models by Nakajima & Ouchi (2014). Compiling literature data, they found an interesting correlation between the emission line ratio [O III]/[O II] (hereafter $\rm O_{32}$) and $f_{\rm esc}$, which they claimed arises when H II regions are "density-bound" and some LyC leakage occurs. This picture contrasts with typical "ionization-bound" H II regions where LyC photons are fully absorbed within the radius of the associated Stromgren sphere. The conjecture has received further support by the recent detections of significant LyC radiation from nearby intense [O III] emitters (Izotov et al. 2016a,b, 2018). The most extreme $\rm O_{32}$ sources in the Nakajima & Ouchi (2014) study were narrow-band selected Lyman alpha emitters (LAEs) whose observed properties are in many respects very similar to the dominant population of star-forming galaxies during reionization. Subsequently, through near-infrared and optical spectroscopy, Nakajima et al. (2016, 2018) provided further evidence that such LAEs have higher values of $\xi_{\rm ion}$ than continuum-selected LBGs (Shivaei et al. 2018).

The most practical route to determine whether early galaxies reionized the IGM is to undertake a detailed study of analogs of this population at the highest redshift where direct measures of $\xi_{\rm ion}$ and $f_{\rm esc}$ are possible. With a representative sample of such analogs it may be possible to verify the inferred correlation between the [O III] emission and $f_{\rm esc}$, as well as to determine the fraction of sources whose ionizing output (as defined by $\xi_{\rm ion}$ and $f_{\rm esc}$) would be sufficient if projected, into the $z > 7$ population, to sustain reionization. Intermediate redshift LAEs possibly represent the most valuable low redshift analogs of the population of compact, low mass, intensely-star forming galaxies that dominate the reionization era. Taking advantage of a large area narrow-band selected sample of spectroscopically-confirmed LAEs in the SSA22 field (Hayashino et al. 2004; Matsuda et al. 2005; Yamada et al. 2012b; Nakajima et al. 2016, 2018), the LACES project (the LymAn Continuum Escape Survey) aims to study these sources in detail and in particular to examine their LyC leakage via Hubble Space Telescope (HST) broad-band imaging below the Lyman limit. A key question our survey can address is whether intense [O III] emission seen in many LAEs is associated with an increased $f_{\rm esc}$ as conjectured originally by Nakajima & Ouchi (2014). Deep UV imaging (and hence measures of $f_{\rm esc}$) is presented for an unique and representative sample of $z \simeq 3.1$ LAE analogs for which the associated measures of Lyα and [O III] are already available from Keck and VLT spectroscopy.

A plan of the paper follows. In Section 2 we introduce our sample which is based on HST imaging in 3 WFC3 fields spanning the area for which we have extensive ground-based optical and near-infrared spectroscopy. In this section we discuss the relevant imaging and spectroscopic data and their processing. In Section 3 we examine the new deep $F336W$ images and devise a procedure for determining the presence of LyC leakage on a case by case basis in our sample, as well as the combined flux from those sources without individual detections. In Section 4 we define a path for deriving the measured $f_{\rm esc}$ or limits on its value from the individual $F336W$ fluxes, noting the dependences on the assumed form of the UV continuum as probed by independent spectroscopic measures of $\xi_{\rm ion}$. In Section 5 we then correlate these measures with various source properties measured either observationally or derived from our model-dependent analyses. In Section 6, we discuss these correlations in the context of whether such [O III]-intense sources are likely prominent agents of cosmic reionization.

Throughout this paper, we adopt a concordance cosmology with $\Omega_\Lambda = 0.7$, $\Omega_m = 0.3$ and $H_0 = 70$ km s^{-1} Mpc^{-1}. All magnitudes are given in the AB system (Oke & Gunn 1983). When we refer to $f_{\rm esc}$ we mean the absolute escape fraction of LyC photons unless specified otherwise.

2. DATA

2.1. *Sample Characteristics and HST Data*

As discussed in Nakajima et al. (2016), our target sample is drawn from a Subaru imaging survey that identified $z \simeq 3.1$ Lyman alpha emitters (LAEs) in the SSA22 field (Hayashino et al. 2004; Matsuda et al. 2005; Yamada et al. 2012b) via their photometric excess in a narrow band filter at 497 nm. In addition to initial spectroscopy to confirm their identity, we have undertaken a systematic campaign using optical spectrographs on Keck and the VLT to study their rest-frame UV emission lines (Nakajima et al. 2018) and near-infrared spectroscopy with Keck's MOSFIRE to examine their rest-frame optical emission, particularly the diagnostic lines of [O III] λ5007 Å and [O II] λ3727 Å. Initial results from

TABLE 1
HST imaging observations

Filter	Pointing	$\lambda_{\rm eff}$ (Å)	PSF[a] ($''$)	Pixel Scale ($''$/pixel)	Exposure (s)	Depth[b] (AB)
$F336W$	1	3355	0.081	0.040	57845	30.18
$F336W$	2	3355	0.081	0.040	57845	30.29
$F336W$	3	3355	0.081	0.040	57845	30.19
$F160W$	All	15369	0.151	0.128	2612	27.61

[a] The FWHM of the PSF.
[b] The 3σ limiting magnitude using an aperture with a diameter 1.5 times the size of the PSF FWHM (e.g. $0.12''$ for the $F336W$ images).

MOSFIRE were presented in Nakajima et al. (2016) but those data have been enlarged in the present paper to take account of the associated imaging data taken with HST.

The HST campaign (GO 14747, PI: Robertson) was conducted between UT 14th May 2017 - 20th December 2017 comprising four $F160W$ pointings with WFC3/IR of 1 orbit each (0.7 hrs) and three WFC3/UVIS $F336W$ pointings of 20 orbits each (16 hrs, see Table 1). Together with the narrow band images taken with Subaru, this strategy allows us to compare prospective Lyman continuum leakage in the $F336W$ filter with associated signals in Lyα and the rest-frame optical continuum.

Within the coverage of the $F336W$ imaging, there are 61 sources from the original Subaru sample of which 54 are LAEs and 7 are LBGs. Although only 41 of the 54 LAEs have spectroscopic redshifts, we can exploit the remaining 13 narrow-band selected sources given contamination from foreground emitters has been shown to be negligible in practice (Matsuda et al. 2005, 2006; Yamada et al. 2012a,b). A summary of the statistical sample is given in Table 3 and their distribution in the 3 WFC3 fields is shown in Figure 1.

The imaging data was reduced using the STScI pipeline and, in the case of the WFC3/UVIS drizzled images, median combined using `SWarp` (Bertin 2010) after background subtraction with appropriate weights. In order to accurately compare $F336W$ detections with signals in other bands, all HST images were astrometrically aligned with the most appropriate Subaru images using the IRAF tools `ccmap` and `ccsetwcs` using bright unsaturated stars. Sources were then extracted in the $F336W$, Subaru NB497 (Lyα) and $F160W$ images using a Python script based on the SEP tool[7] (Bertin & Arnouts 1996; Barbary 2016).

2.2. *Additional Photometry*

All the LACES targets are covered with the plentiful, deep multi-wavelength photometric data in the SSA22 field. We utilize the photometric data including Subaru, CFHT, UKIRT and Spitzer/IRAC imaging data in addition to the HST/$F160W$ photometry to constrain the nature of the stellar populations of the LACES objects via an SED fitting analysis (Section 4.2). Table 2 gives the details of the additional photometric data.

We perform photometry of the bands listed in Table 2 on the LACES sources using TPHOT (v2.0; Merlin et al. 2015, 2016). Briefly, we use the HST/$F160W$ image as a high resolution reference image and extract the spatial and morphological information of objects within a radius of $\sim 25''$ from each of the LACES sources. Using this information and a kernel carefully created to convolve the high resolution image to have the PSF of the lower resolution ground-based images, TPHOT produces templates of the objects in the low resolution image. TPHOT then varies the brightness of each of the templates to match the global observed flux in the low resolution image. In this way we can accurately measure total fluxes from the low resolution images in Table 2 by removing light from nearby contaminating sources. For sources not detected or not covered by the HST/$F160W$ image, we adopt aperture photometry with a $2''$ diameter aperture for the Subaru, CFHT and UKIRT images and $3''$ for the IRAC data and fix the position of the aperture determined using the NB497 detection. The aperture magnitudes are then converted into total magnitudes using aperture correction values, which are estimated from differences between aperture and total magnitudes for point sources. We have confirmed that the two methods return a consistent SED within the 1σ uncertainties for isolated objects.

[7] `https://github.com/kbarbary/sep/tree/v1.0.x`

TABLE 2
Summary of optical and NIR imaging data

Filter	Observatory	PSF ($''$)[a]	Depth (mag)[b]	Reference [c]
$u^\star$	CFHT	1.0	26.0	(1)
B	Subaru	1.0	26.5	(2), (3), (4)
$NB497$	Subaru	1.0	26.2	(2), (3), (4)
V	Subaru	1.0	26.6	(2), (3), (4)
R	Subaru	1.1	26.7	(2), (4)
i'	Subaru	1.0	26.4	(2)
z'	Subaru	1.0	25.7	(2)
J	UKIRT	0.9	23.5	(5)
K	UKIRT	0.8	23.1	(5)
[3.6]	Spitzer	2.0	22.2–24.7	(6)
[4.5]	Spitzer	2.0	22.2–24.4	(6)

[a] The FWHM of the PSF.
[b] The 5σ limiting magnitude using an aperture with a diameter of $3''$ for the IRAC 3.6 and 4.5 μm bands and $2''$ for the other bands.
[c] (1) Hayashino et al. 2018; (2) Hayashino et al. 2004; (3) Yamada et al. 2012b; (4) Matsuda et al. 2005; (5) `http://wsa.roe.ac.uk/`; (6) `http://sha.ipac.caltech.edu/applications/Spitzer/SHA/`

2.3. *Near-Infrared Spectroscopy*

In addition to the initial 2015 campaign reported in Nakajima et al. (2016) which targeted only one MOSFIRE pointing (referred to here as mask 1) in SSA22, we have now completed spectroscopy of three further pointings (masks 2-4) within the HST covered area (Figure 1). The new observations were taken on UT July 31, August 1 and October 10 2017 in photometric conditions with seeing ranging from 0.5-0.9 arcsec in the summer months to 0.3-0.5 arcsec on the more recent run. Spectra were obtained in both the K band (sampling [O III] and Hβ at a spectral resolution $R \simeq 3600$) and H band (sam-

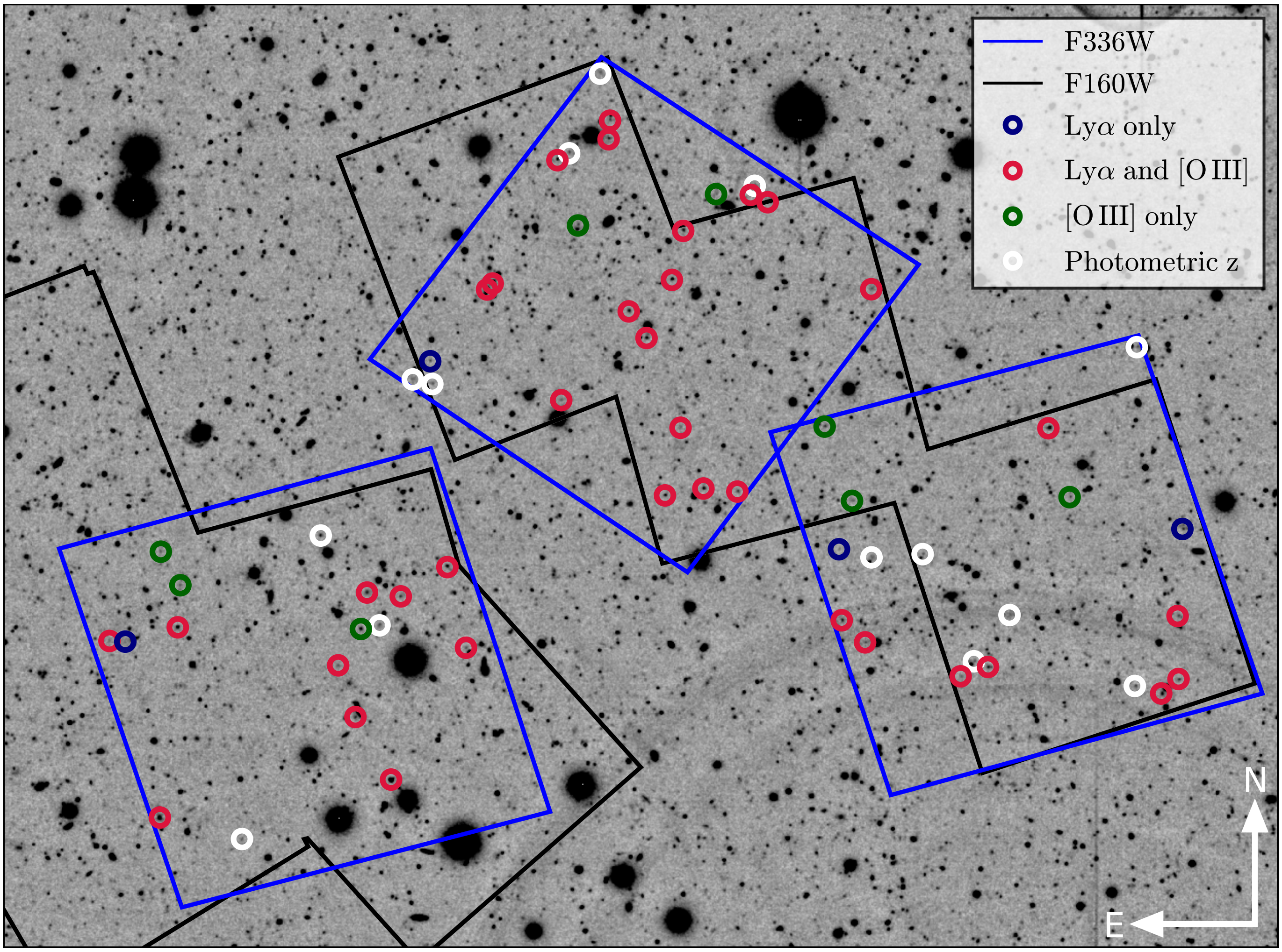

Fig. 1.— NB497 image showing the coverage of target Lyman alpha emitters and Lyman break galaxies from the full Subaru narrow-band selected sample within the three WFC3/UVIS $F336W$ pointings. The area covered by the smaller WFC3/IR $F160W$ pointings are delineated with overlapping black squares. The targets are color-coded according to their information content as follows: (red) Lyα spectroscopic redshift and [O III] line flux, (blue) Lyα spectroscopic redshift only, (green) [O III] spectroscopic redshift only, (white) photometric data only. For detailed statistics see Table 3.

pling [O II] at $R \simeq 3700$) for the masks 1 and 2, while only in the K band for the masks 3 and 4. Individual exposures of 180 sec (120 sec) were taken in K (H) with a AB nod sequence of 3.0 arcsec separation. The total on-source exposure times ranged from 2 to 3 hours with some sources included on both mask 2 and mask 4.

Data reduction was performed using the MOSFIRE DRP[8] in the manner described in Nakajima et al. (2016). Briefly, the processing includes flat fielding, wavelength calibration, background subtraction and combining the nod positions. Wavelength calibration in H was performed using OH sky lines and in K a combination of OH lines and Neon arcs were used. Flux calibration and telluric absorption corrections were obtained from A0V Hipparcos stars observed at similar air masses as well as via relatively bright stars ($K_{\rm Vega} = 15.5$–16.5) included on each of mask.

We measured the [O II] and [O III] line fluxes by fitting a Gaussian profile to each line using the IRAF task `spec fit`. In deriving the rest-frame equivalent width (EW) of [O III], we used the measured $F160W$ in conjunction with a mean spectral energy distribution of $z \simeq 3.1$ LAEs (Ono et al. 2010) to determine the continuum flux in the vicinity of the line near 2.05 μm. We investigated the effect of dust corrections using individually derived $E(B-V)$ values for each object (see Section 4) but as our LAEs are mostly dust-free the corrections were small. Table 3 summarizes the statistics of the [O II] and [O III] detections. The full catalog of line fluxes and equivalent widths will be reported later as the spectroscopic campaign continues.

In total, 51 of the 61 sources in the 3 WFC3 fields have [O III] detections or upper limits. The coverage of [O II] is less complete at present, with roughly half of the [O III] sample containing [O II] data or upper limits (see Table 3).

3. LYMAN CONTINUUM CANDIDATES

We now discuss the procedure adopted to decide which SSA22 sources show promising evidence of Lyman continuum leakage in the HST $F336W$ filter. The key issues include the optimum aperture for measuring the $F336W$ flux, the photometric significance of any detection, the spatial coincidence with signals in other bands and the

[8] https://keck-datareductionpipelines.github.io/MosfireDRP/

TABLE 3
SUMMARY OF THE LACES SAMPLE

N^o of objects	LAEs	LBGs
Within the HST area	54	7
With any form of redshift	41	6
With $F160W$ coverage or limits	45	7
With [O III] or limits	46	7
With [O II] or limits (with [O III] identified)	23	4
With $F160W$ coverage & both [O III]+[O II] data	23	4

possibility of foreground contamination. We also discuss the nature of those sources where no significant $F336W$ flux is seen and examine the possibility of providing a statistical detection on the basis of a stacking analysis.

3.1. *Detections*

We first constructed a mosaic of all 61 targets with HST $F336W$ coverage, comparing the location and morphology of possible $F336W$ detections with images in Subaru NB497 (Lyα), R and HST $F160W$. Three authors (TF, RSE, DPS) examined this mosaic for potential $F336W$ detections. Although the Subaru Lyα image offers a natural astrometric reference point, as a ground-based image with 1 arcsecond seeing it is less useful than the HST $F160W$ image which samples the rest-frame optical light and can reveal complex source morphology. In practice we found it helpful to overlay a $F160W$ contour over the $F336W$ image to evaluate spatial coincidence.

The photometric significance of possible $F336W$ detections was also taken into account on the assumption that LyC signals would be mostly unresolved with HST. Fluxes were measured in an aperture whose diameter is 1.5 times the $F336W$ point spread function (i.e. 3 WFC3/UVIS pixels, 0.12 arcsec, 0.91 kpc at $z = 3.1$). This aperture is more sensitive in discovering candidates than adopting a (larger) matched aperture across all the photometric bands that would introduce unnecessary noise. For the few sources that show extended emission in the $F336W$ image we only measure a signal from the brightest peak, possibly underestimating the true $F336W$ flux and $f_{\rm esc}$.

To evaluate the completeness of our search and provide useful upper limits for the non-detections, we masked all the detected sources above a threshold of 1.5σ of the background noise. Fake sources with a Gaussian profile corresponding to the PSF of the images and known magnitudes were inserted into the unmasked regions and the detection algorithm re-run. In this manner we determined a 75% completeness limit of $F336W(\rm AB) = 29.70$. We verified this noise limit with that determined from aperture measures in the vicinity of each target.

For each LyC candidate the noise level was measured locally in a 4×4 arcsecond region around the target. The targets, neighboring objects and any signal 5σ above the noise level were masked in the postage stamps. Using these segmentation maps apertures 1.5 times the PSF, the same size used to measured the flux, were randomly distributed and the 1σ noise level calculated.

3.2. *Gold and Silver Subsamples*

We have conservatively divided our detections into gold and silver subsamples in order to distinguish between cases where we are respectively convinced and reasonably sure the detected LyC flux is associated with the target galaxy. In our subsequent analysis it will be helpful to examine trends separately between the gold and silver subsamples as well as with those for the non-detections. We show in Figure 2 postage stamps of 4×4 arcsec for our gold and silver subsamples, defined according to the criteria below. Together they comprise 18 sources for which reasonably convincing $F336W$ detections were found by the procedure outlined in Section 3.1. To assist in recognizing the detections, we also show the $F336W$ images smoothed with a 2D Gaussian with 1σ equal to 1 pixel. We also show an overlay of the $F160W$ contours on the $F336W$ images to illustrate the spatial coincidence of the optical continuum and LyC flux.

To qualify for the gold sample, targets must satisfy three criteria:

1. Availability of a spectroscopic redshift for the target or no evidence that the target may be an interloper. A redshift may seem an essential requirement but the probability a NB497 excess which leads to a selected $z = 3.1$ LAE is contaminated by a foreground emission line is very low (Matsuda et al. 2005, 2006; Yamada et al. 2012a,b) so only if there is some spectroscopic evidence for an interloper would the candidate be rejected.

2. The $F336W$ flux must be spatially coincident (to within 0.6 arcsec) with the core of the $F160W$ flux or the Lyα centroid. In cases where the $F160W$ image reveals substructure, there is a danger the $F336W$ detection is coincident with an interloper. Although we will show this possible contamination is unlikely, such a configuration merits demotion to the silver subsample.

3. The $F336W$ detection has a signal to noise $\gtrsim 4$ (to 1 sig. fig.) as evaluated by the process discussed in the next subsection.

Using these criteria we select 9 gold candidates shown in Figure 2. Target IDs 86861, 93564, 90675 and 92616 are all spectroscopically confirmed at $z \gtrsim 3.07$ and are coincident with compact $F160W$ regions, except for 92616 where there is no $F160W$ imaging. In the latter case, the $F336W$ centroid is coincident with the extended Lyα emission. IDs 84986 and 90340 are considered worthy of inclusion because in both the MOSFIRE spectrum no other lines were detected suggesting an interloper is unlikely. IDs 92863 and 100871 were not targeted spectroscopically. Although 100871 also has no $F160W$ imaging, the $F336W$ signal is precisely coincident with the peak of Lyα emission.

We show the silver subsample in Figure 2 for which the primary criterion is a lower $F336W$ signal/noise. Although ID 94460 satisfied all the gold criteria, it is placed in the silver sample because in addition to Lyα, [O III] and $H\beta$ all at $z = 3.07$ an emission line inconsistent with this redshift but spatially offset was found. This may represent evidence for a contaminating source. Likewise the two resolved components in ID 104511 might imply an interloper. IDs 104037 and 105937 fall into the silver sample due to their extended $F160W$ regions. The remainder of the sample has $3 \leq \rm SNR < 4$.

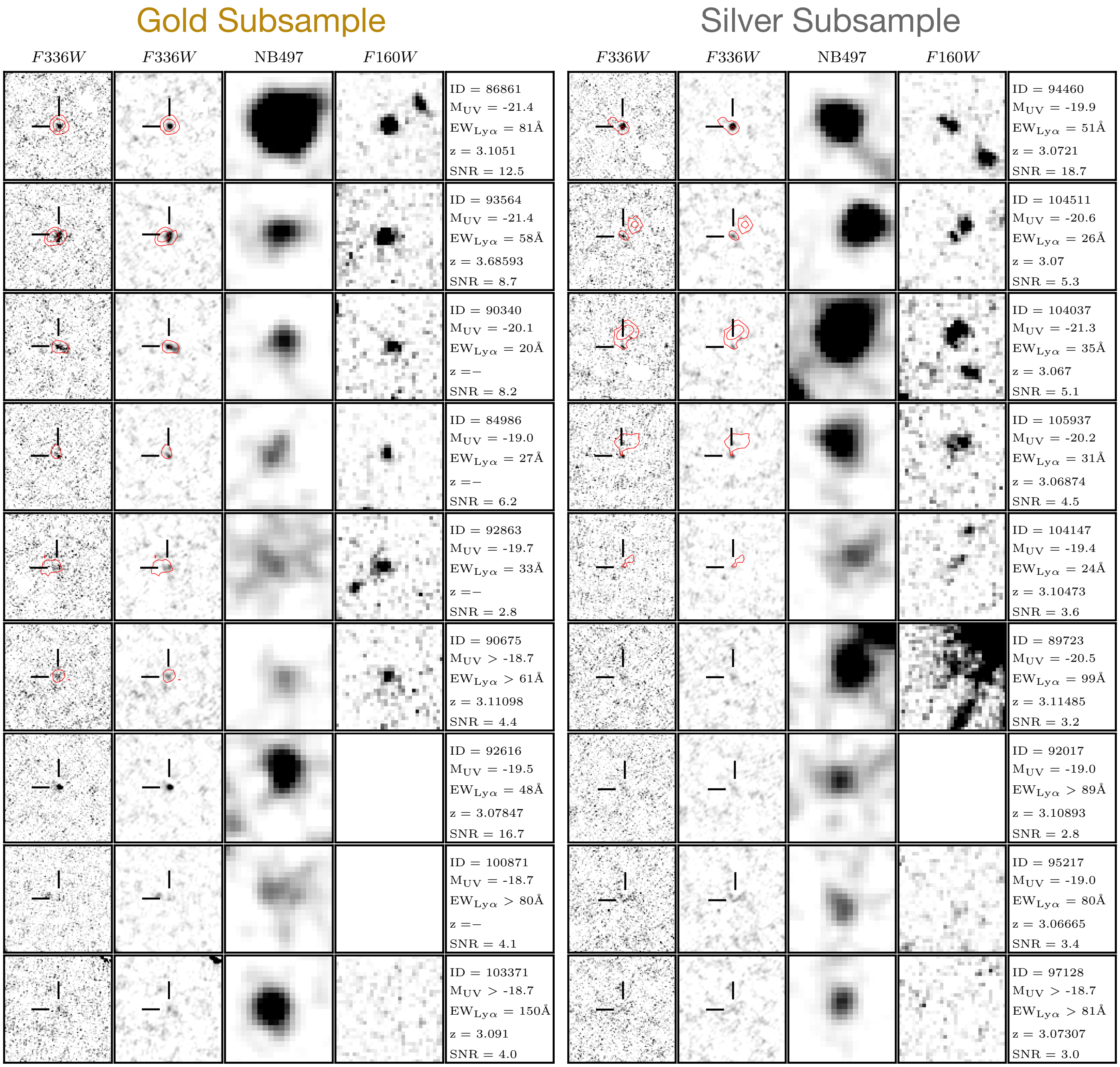

FIG. 2.— Mosaic of astrometrically aligned 4 × 4 arcsec images for 18 sources with high signal to noise *F336W* detections (see text for discussion of the detection procedure) comprising the gold and silver subsamples (left and right columns respectively). From left to right each panel displays (i) the background-subtracted *F336W* image overlaid with contours from the *F160W* image, (ii) the former smoothed, (iii) the Subaru narrow band 497 nm image, (iv) the *F160W* image (where available) and (v) a summary of physical properties where the SNR refers to the F336W detection. All of our objects are LAEs except for 86861 which is a LAE-AGN.

Table 4 summarizes the gold and silver subsamples alongside their photometric and spectroscopic properties. In addition to the two subsamples, we list 3 other promising LyC detections (not shown in either mosaic) whose *F336W* signal/noise ratios are only slightly below the silver threshold of 3.0, or in the case of 107585 had complicated Lyα morphology.

3.3. *Spatial Offsets*

In considering the validity of our sample we now examine two further criteria. The first is the distribution of separations between the *F336W* centroid and that for *F160W* and Subaru Lyα. Although a precise spatial coincidence of LyC leakage and UV/optical continuum and/or Lyα emission is desirable, previous studies have already found the LyC emission is occasionally offset from that of Lyα (Iwata et al. 2009; Mostardi et al. 2013, 2015; Micheva et al. 2017b) with a median separation of $\sim$ 5 proper kpc reported in Mostardi et al. (2015).

Figure 2 indicates that, for the majority of our targets, the *F336W* centroid falls perfectly within the contours from the rest-frame optical (*F160W*) continuum where available. Figure 3 shows the distribution of spatial offsets between *F336W* and both the Lyα and *F160W* centroids. For 85% of the candidates, the separation be-

TABLE 4
Properties of the LyC Leaking Candidates

ID	$f_{\rm Lyc}$ (10^{-9}Jy)	SNR	$M_{\rm UV}$	EW(Lyα) (Å)	$z_{\rm sys}$	$\Delta v_{\rm Ly\alpha}$ (km s^{-1})	EW([O III]) (Å)	[O III]/Hβ	R23	[O III]/[O II]
Gold Sample										
86861*	13.0	12.6	-21.4 ± 0.0	81^{+2}_{-2}	3.1051	338.9	322.0 ± 15.5	10.1 ± 3.4	10.1 ± 3.4	> 5.6
93564	8.3	8.8	-21.4 ± 0.0	58^{+6}_{-6}	3.6768	585.3	1129.7 ± 36.5	8.9 ± 0.8	9.8 ± 0.9	10.8 ± 2.0
90340	8.3	7.9	-20.1 ± 0.1	20^{+7}_{-6}	–	–	< 80.5	–	–	–
84986	5.8	6.3	-19.0 ± 0.3	27^{+13}_{-10}	–	–	< 242.5	–	–	–
92863	4.6	4.2	-19.7 ± 0.2	33^{+12}_{-9}	–	–	–	–	–	–
90675	4.2	4.1	> -18.7	> 61	3.1108	10.9	–	< 0.6	–	–
92616	15.6	17.3	-19.5 ± 0.2	48^{+12}_{-10}	3.0713	265.1	–	> 3.5	–	–
100871	3.6	4.7	> -18.7	> 80	–	–	–	–	–	–
103371	4.3	4.0	> -18.7	150^{+71}_{-46}	3.0892	-2.2	> 1578.8	8.7 ± 2.3	8.7 ± 2.3	> 7.0
Silver Sample										
94460	15.8	18.4	-19.9 ± 0.1	51^{+8}_{-7}	3.0721	171.5	432.1 ± 22.6	8.5 ± 1.6	8.5 ± 1.6	> 7.5
104511	5.6	5.3	-20.6 ± 0.1	26^{+4}_{-3}	3.0647	–	1346.8 ± 45.3	8.1 ± 0.9	–	–
104037	4.8	5.2	-21.3 ± 0.0	35^{+2}_{-2}	3.0646	194.7	932.5 ± 21.1	14.5 ± 1.1	16.9 ± 1.2	6.0 ± 0.3
105937	5.2	4.5	-20.2 ± 0.1	31^{+7}_{-6}	3.0670	128.3	103.8 ± 13.9	> 3.1	–	–
104147	3.1	3.5	-19.4 ± 0.2	24^{+7}_{-6}	3.0991	415.4	409.5 ± 65.4	> 8.6	> 8.6	> 5.7
89723	3.2	3.2	-20.5 ± 0.1	99^{+25}_{-20}	3.1109	285.9	–	> 7.2	> 7.2	> 3.3
92017	2.4	2.8	-19.0 ± 0.3	> 89	3.1069	151.1	–	> 3.2	–	–
95217	3.4	3.2	-19.0 ± 0.3	80^{+49}_{-32}	3.0667	–	1057.1 ± 394.2	> 2.0	> 2.0	> 1.1
97128	3.2	3.0	> -18.7	> 81	3.0731	–	> 5372.7	1.6 ± 0.5	–	–
Other Candidates										
107585†	4.6	5.2	-19.3 ± 0.2	24^{+11}_{-8}	3.0892	–	–	3.5 ± 0.9	–	–
89114	3.0	2.6	-19.6 ± 0.2	39^{+10}_{-8}	3.0834	-320.8	1358.7 ± 124.7	> 6.9	< 25.39	< 53.88
106500	2.8	2.8	-19.3 ± 0.2	89^{+40}_{-30}	3.0584	–	1869.8 ± 289.3	4.6 ± 0.6	25.92 ± 0.09	54.28 ± 0.05

SNR ≥ 3 is required for a detection. The columns (numbered) denote the following: (1) LyC Flux. (2) Signal-to-noise ratio. (3) Absolute UV magnitude. (4) Rest equivalent width (EW) of Lyα. For the $z \simeq 3.1$ objects, the EW is estimated from the BV−NB497 color in conjunction with the Lyα redshift. The EW of LAE93564 is derived from spectroscopy. (5) Systemic redshift measured from the [O III] and Hβ line(s). (6) Velocity offset of Lyα, $(z_{\rm Ly\alpha} - z_{\rm sys})/(1 + z_{\rm sys}) \times c$. (7) Rest EW of [O III] $\lambda\lambda5007, 4959$. The associated continuum is estimated from HST/$F160W$ photometry, which is translated into the flux density at 5000 Å with the typical SED of $z \sim 3$ LAEs (Ono et al. 2010). (8) [O III] $\lambda\lambda5007, 4959$/Hβ. (9) R23-index. (10) [O III] $\lambda\lambda5007, 4959$/[O II] $\lambda3727$. No reddening correction has been applied to the Oxygen and Hβ values presented here as the reddening correction is very small (see Table 5). The $*$ denotes the one LAE-AGN in our sample. Objects 86861, 93564 and 94460 are reported respectively as AGN04, LBG01 and LAE06 in Micheva et al. (2017a,b). (†) 107585 is a very promising LyC leaker. However, due to the complex Lyα morphology and in the absence of $F160W$ coverage for this object it is difficult to identify the spatial coincidence of the LyC signal with the LAE.

tween the LyC and $F160W$ centroid is less than 0.4 arcseconds (3 proper kpc at $z = 3.1$). For reference $1''$ at $z = 3.1$ corresponds to 7.6 proper kpc. The angular resolution of the ground-based NB497 images is naturally worse. However for all of our candidates the $F336W$ emission lies within $0.8''$ (6.1 proper kpc) of the Lyα centroid which we consider satisfactory given the seeing in the Subaru image is $\simeq$1.0 arcsec.

In fact, targets with larger LyC - $F160W$ separations tend to have extended $F160W$ or Lyα emission, or in the case of ID 104511, several components. In these cases the LyC emission is still coincident but, due to the extended nature of the source, it can fall further from the centroid in the NB497 or $F160W$ bands. If LyC photons are emitted from regions occupied by young stars, then LyC may reasonably lie closer to the rest-frame optical compared with Lyα that may be resonantly scattered. These small separations are encouraging and lead us to believe the putative $F336W$ detections are due to LyC photons emitted from LAEs at $z \simeq 3.1$.

3.4. *Foreground Contamination*

Although we have attempted to isolate candidates whose $F336W$ detections may arise from foreground contaminants, we can estimate statistically the likelihood of

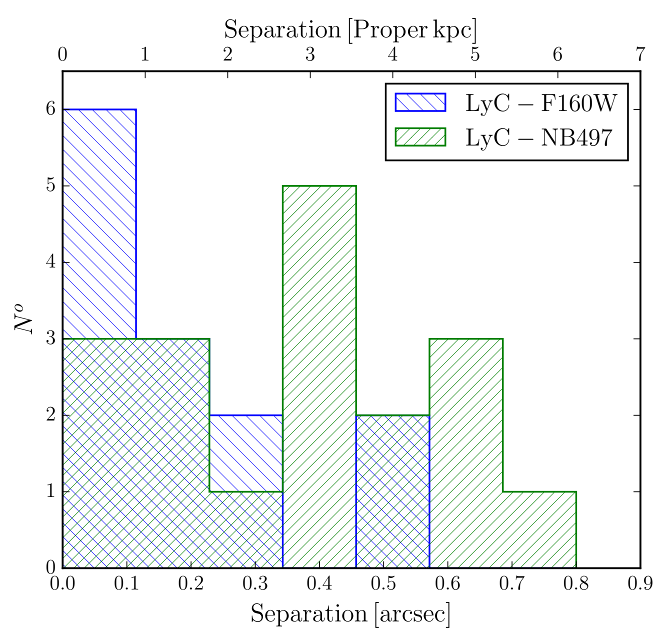

Fig. 3.— Distribution of separations between the peak of the LyC emission and the peak of both the Lyα (18 cases) and $F160W$ emission (when available, 13 cases).

interlopers from luminosity functions of lower redshift galaxies. The relevant calculation requires, as input, the aperture within which LyC flux is searched. As a result, estimates of contamination must account for the possibility that the most active star-formating regions from which LyC photons are emitted could be spatially offset from the bulk of the stars and gas in the galaxy. This effect has been discussed in both ground-based studies (Iwata et al. 2009; Inoue et al. 2011; Nestor et al. 2011, 2013) and those using HST (Mostardi et al. 2015). Allowing for spatial offsets increases the effective aperture and hence increases the likelihood of foreground contamination. In addition, the likelihood of contamination decreases with the depth and resolution of the imaging data. Fortunately, in our case, deep WFC3 UVIS/$F336W$ imaging provides the best angular resolution possible and probes to depths of 30.2 AB magnitudes.

Following the method of Vanzella et al. (2010), we now calculate the probability a single source is contaminated and the probability N of our 18 detections suffer from foreground contamination. We use the number counts per deg^2 in Vanzella et al. (2010) derived from the ultra-deep VIMOS U band imaging taken in the GOODS-S field (Nonino et al. 2009). As our $F336W$ measurements are very deep we use the 3σ upper limits for the faintest U band magnitudes up to 30.5 AB (Vanzella et al. 2010). We adopt two aperture sizes for this calculation consistent with the distribution of offsets between LyC - $F160W$ and LyC - NB497 shown in Figure 3: (i) a $0.24''$ diameter aperture which corresponds to most coincident cases, and (ii) a $0.80''$ diameter aperture which encompasses all the offsets measured for the gold and silver subsamples. The $0.24''$ aperture is used where the separation between the LyC centroid and either of the $F160W$ or Lyα centroid is $\leq 0.24''$ ($N = 9$). For objects where both Lyα and the $F160W$ centroid is $> 0.24''$ from the LyC emission we use the $0.80''$ aperture ($N = 9$). Using these two apertures for the relevant LyC detections, we estimate the contamination rate for single sources to vary between $0.7 - 2.1\%$ and $7.9 - 20.6\%$ for the smaller and larger apertures respectively.

In Figure 4 we combine these individual estimates for contamination and run Monte Carlo simulations to show the probability that N of the 18 candidates could be contaminated. The probability that 0, 1, 2 or 3 of our 18 candidates could be contaminated is 54%, 22%, 15% and 6% respectively. Indeed, in 97% of cases we estimate that ≤ 3 of our LyC detections could be contaminated. We cannot rigorously perform the same analysis on the non-detections as we are cannot measure the possible offsets between LyC and Lyα and $F160W$ centroids. However, if we assumed a similar distribution of offsets, applying the same analysis to all 51 LAEs would still predict far fewer potential contaminants than the number of detections we report for the LACES sample. We therefore have detected LyC escape directly.

3.5. *Non-Detections*

The majority (33 of 54) of our LAEs have no clear $F336W$ detections above a signal to noise ratio of 3. To determine if these non-detections simply represent a tail of fainter signals, we can stack the non-detections to derive a statistical estimate of their mean $F336W$ flux. In

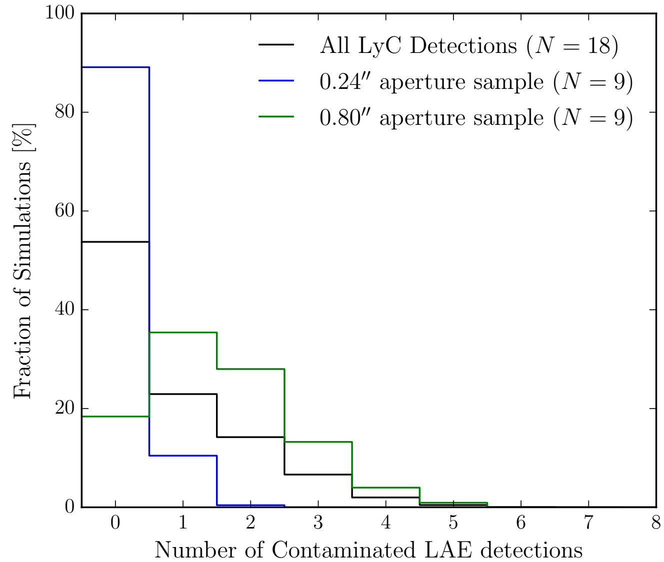

Fig. 4.— Probability distribution of contamination in our sample of 18 detected objects. The probability N of the 18 objects is contaminated is shown for 0.24 and 0.80 arcsecond apertures. In 97% of cases ≤ 3 of the 18 LyC detections are predicted to be affected by contamination.

this case, we must first consider how to register the images, recognizing that the LyC flux may not always precisely coincide with either the $F160W$ or Lyα signals (Figure 3). We can evaluate the impact of such spatial offsets by conducting the same stacking experiment on those sources for which we see individual detections. By comparing the stack for the gold and silver subsamples based on different registrations ($F160W$ and Lyα), we can compare the loss in stacked signal compared to a direct sum of the registered $F336W$ detections.

For the following stacking procedure, we used the IRAF tool `imcombine` and performed a clipped average stack centered on the position of either the $F336W$ peak (for the gold and silver subsamples), the Subaru NB497 Lyα peak and the HST $F160W$ peak.

The results for the detected (gold and silver) subsamples are shown in Figure 5. As expected using the $F160W$ centroid generally gives a better S/N ratio in the final stack and there is little degradation in signal compared to a direct summation of the $F336W$ signals, especially for the gold subsample. This correspondence simply reflects the small spatial offsets involved.

Applying the same procedure now to the 32 $z \simeq 3.1$ LAEs not detected individually in $F336W$, we can only register using the Lyα and $F160W$ centroids. Surprisingly however, no stacked signal is detected regardless of the centroiding method. In Section 6.1 we later eliminate the hypothesis that the non-detected sources are drawn from a different population to the 18 detections presented in Figure 2, since they sample the same range of M_{UV}, $EW_{Ly\alpha}$, $EW_{[O\,III]}$ and $\Delta v_{Ly\alpha}$, as shown in Figure 14. Likewise the issue of spatial offsets e.g. LyC - $F160W$ inherent in any sample should not preclude a faint $F336W$ detection since it does not significant weaken the stacked $F336W$ signal in the gold or even silver subsamples (Figure 5). The inevitable and remarkable conclusion, therefore, is that the mean $F336W$ signal in the non-detected sample must be uniformly much fainter than for the detected sample. Quantitatively we can say that the 3σ

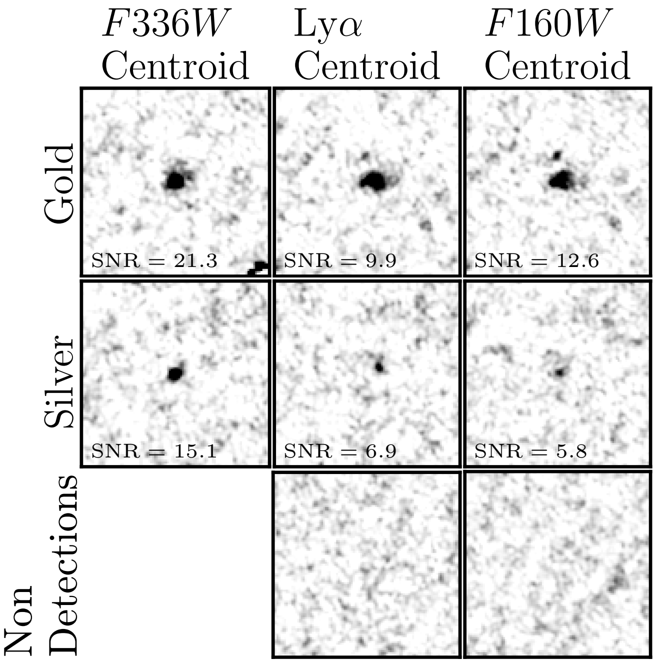

FIG. 5.— Mosaic of 4×4 arcsec images showing stacked $F336W$ images for the gold (top row), silver (middle row) and non-detections (bottom row) samples using different methods to center on the candidate galaxies. From left to right each panel displays the detections stacked using (i) $F336W$ centroid, (ii) Lyα centroid, (iii) $F160W$ centroid or Lyα centroid for cases where $F160W$ is unavailable.

upper limit for the $F336W$ stack of 32 non-detections is 31.6 (AB). Thus it appears the $F336W$ flux in our total sample is either detected individually or not at all. We defer discussion of this important result to Section 6.

4. ANALYSIS

We now turn to using our $F336W$ detections and upper limits to derive the escape fraction $f_{\rm esc}$ of ionizing photons, both on a galaxy-by-galaxy basis for our sample and for the population as a whole. We likewise seek to correlate the escape fractions with our infrared spectroscopic measures of [O III] emission, primarily to test the hypothesis that a high escape fraction is connected with the intense [O III] emission that seems commonplace for star-forming sources in the reionization era.

4.1. *Relative Escape Fractions*

Estimating the escape fraction of Lyman continuum photons requires knowledge about the intrinsic source spectrum before attenuation by interstellar dust in the rest-ultraviolet or by the intergalactic medium blueward of Lyman-α. We can use SED modeling to constrain the escape fraction while simultaneously fitting for other galaxy parameters on a source-by-source basis, and we perform that analysis below. However, given the additional uncertainties and model dependencies associated with SED fitting, we now consider estimates of the escape fraction derived directly from the source photometry.

The relative escape fraction of Lyman continuum photons, $f_{\rm esc,rel}({\rm LyC})$, is often defined in terms of the source flux f_{900} at $\lambda_{\rm rest} = 900$ Å and the rest-ultraviolet flux f_{1500} at $\lambda_{\rm rest} = 1500$ Å as

$$f_{\rm esc,rel}({\rm LyC}) = \frac{(f_{900}/f_{1500})}{(L_{900}/L_{1500})t_{\rm IGM}}, \qquad (1)$$

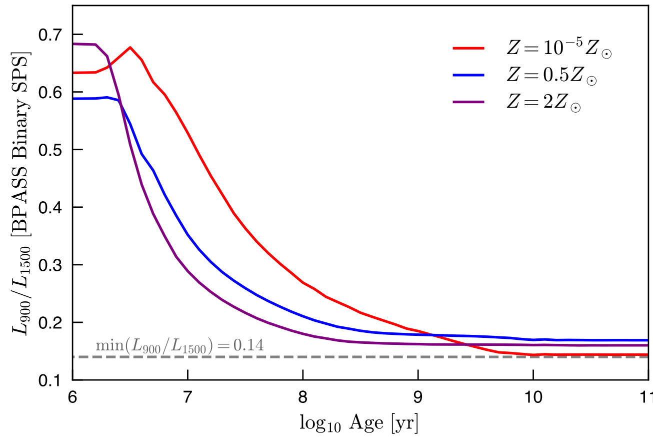

FIG. 6.— The ratio L_{900}/L_{1500} of the luminosity density at 900 Å and 1500 Å for constant star formation rate BPASS binary stellar population models as a function of age, for metallicities of $Z = 10^{-5}Z_\odot$ (red), $Z = 0.5Z_\odot$ (blue), and $Z = 2Z_\odot$ (purple). For typical ages and metallicities of real galaxies, the luminosity density ratio falls in the range $0.15 \lesssim L_{900}/L_{1500} \lesssim 0.3$. For the estimated relative escape fractions inferred directly from the observed source flux ratios, we will adopt a minimum ratio of $\min(L_{900}/L_{1500}) = 0.14$ (dashed gray line).

where (L_{900}/L_{1500}) is the ratio of the intrinsic spectrum at $\lambda_{\rm rest} = 900$ Å and $\lambda_{\rm rest} = 1500$ Å and $t_{\rm IGM}$ is the transmission fraction in the Lyman continuum through the IGM (e.g., Steidel et al. 2001; Inoue et al. 2005; Shapley et al. 2006). Clearly both (L_{900}/L_{1500}) and $t_{\rm IGM}$ are model-dependent quantities, and reflect assumptions about the intrinsic stellar population spectrum and the range of IGM absorption properties.

Here, we aim to provide an estimate of the relative escape fraction that is easily interpreted before turning to a more sophisticated estimate derived from the full set of photometric data. We therefore define the estimated relative escape fraction

$$\tilde{f}_{\rm esc,rel}({\rm LyC}) = \frac{(f_{F336W}/f_R)}{\min(L_{900}/L_{1500})\langle t_{\rm IGM}\rangle}. \qquad (2)$$

Here we replace the measured flux ratio (f_{900}/f_{1500}) with our closest photometric flux ratio measure (f_{F336W}/f_R) using the $F336W$ and R bands. The quantity $\langle t_{\rm IGM}\rangle$ is the mean IGM transmission fraction and, using the Inoue et al. (2014) IGM absorption model, we find that for our $z \sim 3.1$ emitters $\langle t_{\rm IGM}\rangle \approx 0.53$. We then need to define the quantity $\min(L_{900}/L_{1500})$, the minimum intrinsic luminosity density ratio expected for the source stellar populations. We choose to use the minimum luminosity density ratio in Equation 2 to provide upper limits on $\tilde{f}_{\rm esc,rel}({\rm LyC})$ for our choice of $\langle t_{\rm IGM}\rangle$. As we will see the estimated relative escape fraction can be $\tilde{f}_{\rm esc,rel}({\rm LyC}) > 1$, which physically requires stellar populations with ages $t < 10^9$ yr and/or a low opacity sight line through the IGM.

Figure 6 shows the intrinsic ratio of the Lyman continuum and rest-UV luminosity densities for constant star formation rate binary stellar population models computing using Version 2.1 of the Binary Population and Spectral Synthesis (BPASS) code (Eldridge & Stanway 2009, 2012; Stanway et al. 2016; Eldridge et al. 2017). We compute the intrinsic ratio as a function of stellar population age in the BPASS models, and plot the quantity for metallicities $Z = [10^{-5}Z_{\odot}, 0.5Z_{\odot}, 2Z_{\odot}]$ assuming an upper stellar mass limit of $M = 100M_{\odot}$. For galaxies with stellar population ages older than 10^8 years, the typical ratio will be $0.15 \lesssim L_{900}/L_{1500} \lesssim 0.3$. Motivated by the behavior of these models, for our estimated relative escape fraction $\tilde{f}_{\rm esc,rel}$ we adopt the value $\min(L_{900}/L_{1500}) = 0.14$.

With concrete values for the quantities in the numerator of Equation 2, we can use the measured $F336W$ and R band fluxes to estimate $\tilde{f}_{\rm esc,rel}$. Figure 7 shows the estimated relative escape fraction for our LAE sources as determined by the $F336W$ and R band flux ratios, assuming $\min(L_{900}/L_{1500}) = 0.14$ and $\langle t_{\rm IGM}\rangle \approx 0.53$. The uncertainties on the estimated relative escape fraction are computed by propagating the uncertainties on the measured fluxes. The $\tilde{f}_{\rm esc,rel}$ values for individual sources are listed in Table 5, and fall in the range $\tilde{f}_{\rm esc,rel} \approx 0.1 - 1.5$.

4.2. *SED Model Fits*

The absolute escape fraction is conventionally defined as the ratio of those LyC photons emerging compared to those intrinsic to the stellar population. A first necessary step, therefore, is to determine the most likely stellar population and dust extinction for each source from which the intrinsic LyC radiation can be predicted. Fortunately, the SSA22 sample has extensive multi-band photometry, and so the SEDs of many galaxies are well-constrained and provide the basis for this important step. A second requirement is to correct the detected $F336W$ flux upward to allow for line of sight absorption in the IGM. The mean IGM opacity increases as a function of redshift, and may vary between sources owing to fluctuations in the number of absorbers along the line of sight.

We begin by fitting the SEDs of all the sources in our sample, regardless of whether they have $F336W$ detections. The SED data comprises U-band data from the Canada-France-Hawaii telescope, B, V, R, i and z from Subaru, J and K from UKIRT as well as $F160W$ from HST and full 4 Channel coverage from IRAC on-board the Spitzer Space Telescope. These precursor datasets are summarized in Table 2 and the individual photometry is shown in Table 7.

We use BPASS v2.1 to generate synthetic spectral energy distributions that we fit to the data[9]. Assuming a constant star formation history, $Z = 0.1Z_{\odot}$ metallicities, and stellar masses in the range $M \in [0.1, 100]M_{\odot}$[10], we couple the BPASS models with the *MULTINEST* (Feroz & Hobson 2008; Feroz et al. 2009) nested sampler to perform Bayesian parameter estimation on each galaxy's star formation rate ($A_{\rm SFR} \in [0, 100]M_{\odot}/{\rm yr}$), stellar age ($t_{\rm age} \in [0, t_{\rm max}(z)]$), dust extinction assuming the Gordon et al. (2003) Small Magellanic Cloud reddening law, and the escape fraction ($f_{\rm esc} \in [0, 1]$). When performing parameter estimation, we use flat priors for $A_{\rm SFR}$, $t_{\rm age}$, and $f_{\rm esc}$. When estimating the reddening, we adopt a zero-mean Gaussian prior on $E(B-V)$ with an rms $\sigma_{E(B-V)} = 0.05$. When fitting the BPASS SEDs to the photometry we have examined both single and binary star stellar populations, and report results for binary population models since these fits produce conservatively lower inferred $f_{\rm esc}$. Nebular continuum and line emission is included following the precepts of Robertson et al. (2010), with the strength of the nebular emission scaling with the Lyman continuum photon production rate and moderated by the escape fraction. Attenuation from the intergalactic medium owing to neutral hydrogen absorption is included following Inoue et al. (2014), and is applied according to the spectroscopic redshift of each source (or the narrow band Lyα redshift if spectroscopy was unavailable). When fit, the escape fraction simply adjusts the model $F336W$ flux by a multiplicative factor and we incorporate any possible dust attenuation of the Lyman continuum into the value of $f_{\rm esc}$. Model photometry is calculated from the model spectra following Papovich et al. (2001).

Figures 8 and 9 show model SED fits to the individual gold and silver subsample objects. For each object, the maximum likelihood model parameters for star formation rate, stellar age, $E(B-V)$, and escape fraction are indicated. Inset panels in the figures indicate the marginal distribution for f_{esc} determined from each model fit. The SED parameter constraints are recorded in Table 5, which lists the mean and 1σ width of the posterior distributions [11]. The quality of the fits vary depending on the photometric constraints available for each object, and the constraints on f_{esc} vary correspondingly. The typical escape fractions inferred from individual SED fits are $f_{esc} \approx 0.4$ for the gold subsample and $f_{esc} \approx 0.3$ for the silver subsample, with substantial spread.

4.2.1. *SED Model Tests*

The SED modeling provides stellar population constraints on the objects, and enables a model-dependent inference of the escape fraction f_{esc}. While the details of the model do not change whether Lyman continuum flux is detected in our sample and could not permit a conclusion that $f_{esc} \sim 0$, assessing the influence of our model assumptions on our derived parameters is important. We consider some important potential issues below.

Rest-Frame UV and Optical Photometry: The rest-frame optical photometry provides constraints on the presence of evolved stellar populations and, for some combinations of redshifts and photometric bands, the possible influence of nebular line emission. Without constraints on the escaping Lyman continuum flux, the permitted contribution of internally absorbed Lyman continuum photons to the nebular emission can vary widely. Whether the $F336W$ or IRAC fluxes influence the stellar population parameters therefore depend on the detailed shape of the object SED. For instance, gold Object 86861 has a model escape fraction of $f_{esc} = 0.43 \pm 0.04$ when including all the photometric data. The rest-frame UV, $F160W$, and IRAC data for this object provide reasonably tight constraints on the object parameters, such that if the $F336W$ data is removed from the fit, the star for-

[9] Although one of our gold subsample objects (86861) is a weak LAE-AGN, from here onwards we proceed in using the BPASS models for consistency with the rest of our LAEs.

[10] Models with a $300M_{\odot}$ cut-off increase the ionizing flux by $\sim 5\%$ (Eldridge et al. 2017) given the same rest-frame UV luminosity. The choice of model will therefore introduce a $\sim 10\%$ uncertainty in $f_{\rm esc}$.

[11] The error reported here is inferred from the posterior distribution, but does not include systematic effects associated with model uncertainties.

mation rate and age of the object only change less than 5% to $A_{\rm SFR} = 8.3\ M_\odot$/yr and $\log_{10} t_{\rm age} = 8.9$. However, the IRAC data for this object does help resolve the age-SFR degeneracy and removing the IRAC data decreases the age to $\log_{10} t_{\rm age} = 8.3$, increases the star formation rate to $A_{\rm SFR} = 9.6\ M_\odot$/yr, and decreases the inferred escape fraction to $f_{esc} = 0.38$. For other objects with good photometric constraints in the rest frame UV and at $F160W$, such as silver Object 104037, the escape fraction constraints can change by less than 20% when the IRAC photometry is ignored.

IGM Absorption: Without considering additional possible constraints on the ionizing emissivity of the LAEs, the escape fraction inferred by the SED modeling will directly anti-correlate with the IGM attenuation along the line of sight to any object. Models of the IGM absorption by Madau (1995) or Inoue et al. (2014) connect the IGM absorption with the occurrence of neutral hydrogen systems along the line of sight, and variations in the absorption to the statistical variance of these absorbers (e.g., Inoue & Iwata 2008). Since the escape fraction is bounded in the range $f_{esc} \in [0, 1]$ and the IGM absorption depends exponentially on the line-of-sight opacity, the detection of the Lyman continuum in multiple objects may suggest that our SSA22 line-of-sight has lower than average opacity. If the IGM transmissivity is higher than the average $\langle t_{\rm IGM} \rangle \approx 0.5$ we assume, then our inferred escape fractions could go down by a factor of two at most. Given that we find a substantial spread in the inferred f_{esc} for our objects, we can only conclude that the IGM transmissivity is not uniformly low.

Stellar Population Binarity: We assume binary stellar populations in the BPASS models. For a constant star formation rate population with an age $t_{\rm age} > 100$ Myr, the difference in the Lyman continuum flux per unit UV luminosity density is only $\Delta \log_{10} \xi_{ion,0} \sim 0.05$ for $Z = Z_\odot/10$ and the difference overall production rate of Lyman continuum photons is $\Delta \log_{10} N_{\rm ion} \sim 0.1$. The differences in f_{esc} inferred from changing between single and binary stellar populations therefore vary less than the typical uncertainties associated with star formation history, dust, and age.

Dust Model: Variations in the dust model can influence the escape fraction inferred from SED modeling, as the absorption in the rest-frame UV for a given $E(B-V)$ can differ and result in different ratios between the intrinsic model and observed Lyman continuum fluxes. Many of our objects are very blue and permit only very small values of $E(B-V)$, but in a handful of cases the best-fit $E(B-V) \gtrsim 0.1$ for SMC dust. For instance, our gold subsample object 92863 has an inferred SMC $E(B-V) = 0.07$. Using a Calzetti et al. (1994) dust law results in an $E(B-V) = 0.07$, but the best-fit star formation rate has declined by 40% to $A_{\rm SFR} = 3.1\ M_\odot$/yr, the age has increased to $\log_{10} t_{\rm age} = 9.3$, and the inferred escape fraction increases substantially to $f_{\rm esc} = 0.39$. However, these changes represent only $\sim 2\sigma$ changes compared to the SMC dust-based model parameter constraints, and while objects with non-negligible dust may have a systematic uncertainty associated with the dust model their SED fits tend to be less constrained anyway. Fortunately, our sample of intrinsically blue LAEs will suffer less from the systematic uncertainties associated with dust than Lyman continuum surveys of more evolved LBG samples.

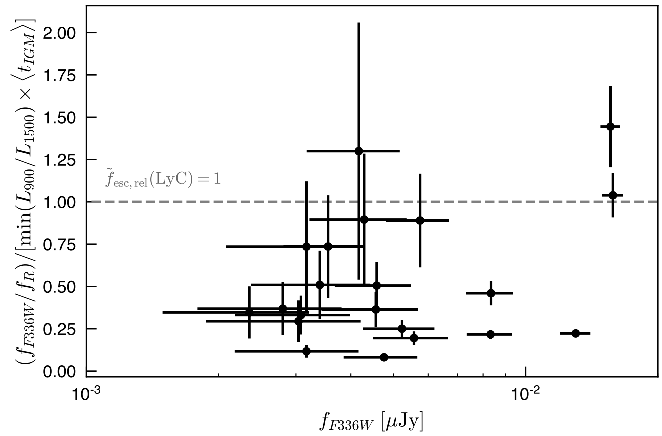

FIG. 7.— Estimated relative escape fractions $\tilde{f}_{\rm esc,rel}$ for our LAE sample, as a function of the detected $F336W$ flux. Shown are the flux ratios f_{F336W}/f_R (black points) normalized by the minimum intrinsic luminosity density ratio $\min(L_{900}/L_{1500}) = 0.14$ and the mean IGM transmission fraction $\langle t_{\rm IGM} \rangle \approx 0.53$. The vertical error bars indicate the uncertainty on the estimated relative escape fractions owing to the individual uncertainties on the measured $F336W$ and R band fluxes, while the horizontal error bars correspond to the uncertainties on the $F336W$ flux. For objects above $\tilde{f}_{\rm esc,rel} = 1$ (gray dashed line), young stellar populations ($t \lesssim 10^9$ yr) and/or lower-than-average IGM absorption are required.

4.3. *Measured vs. Model Line Fluxes*

The SED models are fit to the observed photometric fluxes for each source, but our spectroscopic campaign has also provided independent measures of the fluxes of Hβ, and [O III] that can be used to assess the validity of the model line emission that we incorporate in the rest-frame optical source SED. In the case of Hβ, examining the ratio of the model line flux to that observed for a range of the Lyman continuum photon production rate, we find $\langle f_{mod}/f_{obs} \rangle = 1.44 \pm 1.81$. Since the model line fluxes depend on $(1 - f_{esc,\rm SED})$ determined from the SED fit, this illustrates the degree of self-consistency between the observed and modeled Lyman continuum flux, the inferred escape fractions $(1 - f_{esc,\rm SED})$, and the method for computing the model line strengths that contribute to the photometric data.

4.4. *Composite SEDs*

The photometry of our sources derives from a combination of ground and space-based imaging, with a range of sensitivity and spatial resolution. Excepting $F336W$, the rest-frame UV measurements all come from ground-based data. While this data is of high quality, for some objects it permits a range of stellar population parameters that provide statistically similar model fits. Various combinations of star formation rate and age can produce the same rest-UV flux given these uncertainties, but would lead to a range of inferred f_{esc} as illustrated by the marginal distributions shown in Figures 8 and 9. Given the homogeneity of our sample objects and their comparable redshifts, we have constructed composite photometry for the gold, silver, and $F336W$ Non-Detection subsamples and performed SED model fits to the composite data.

The composite SEDs were generated by first cutting out 6×6 arcsecond postage stamps, centered on the R

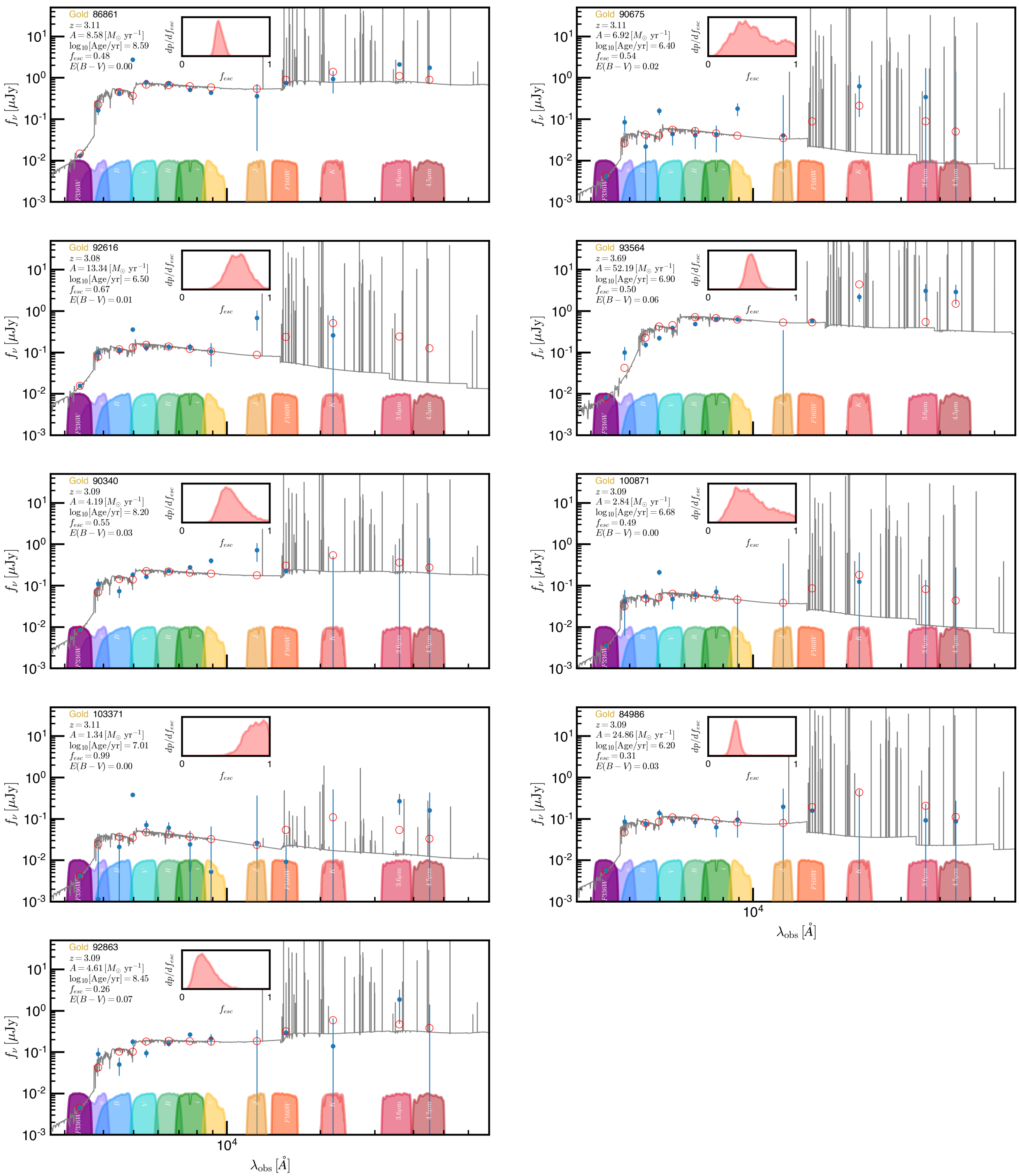

Fig. 8.— SED fits to gold subsample $z \simeq 3.1$ LAEs. The photometric data (blue points with error bars) for each source across 12 bands (colored regions) is used to constrain the SED model fit (gray line), resulting in the model photometry (open red circles). The maximum likelihood parameters for the star formation rate, the age of the constant star formation rate stellar population, the extinction, and the Lyman continuum escape fraction are reported. The insets show the marginal constraint on the escape fraction f_{esc} for each object.

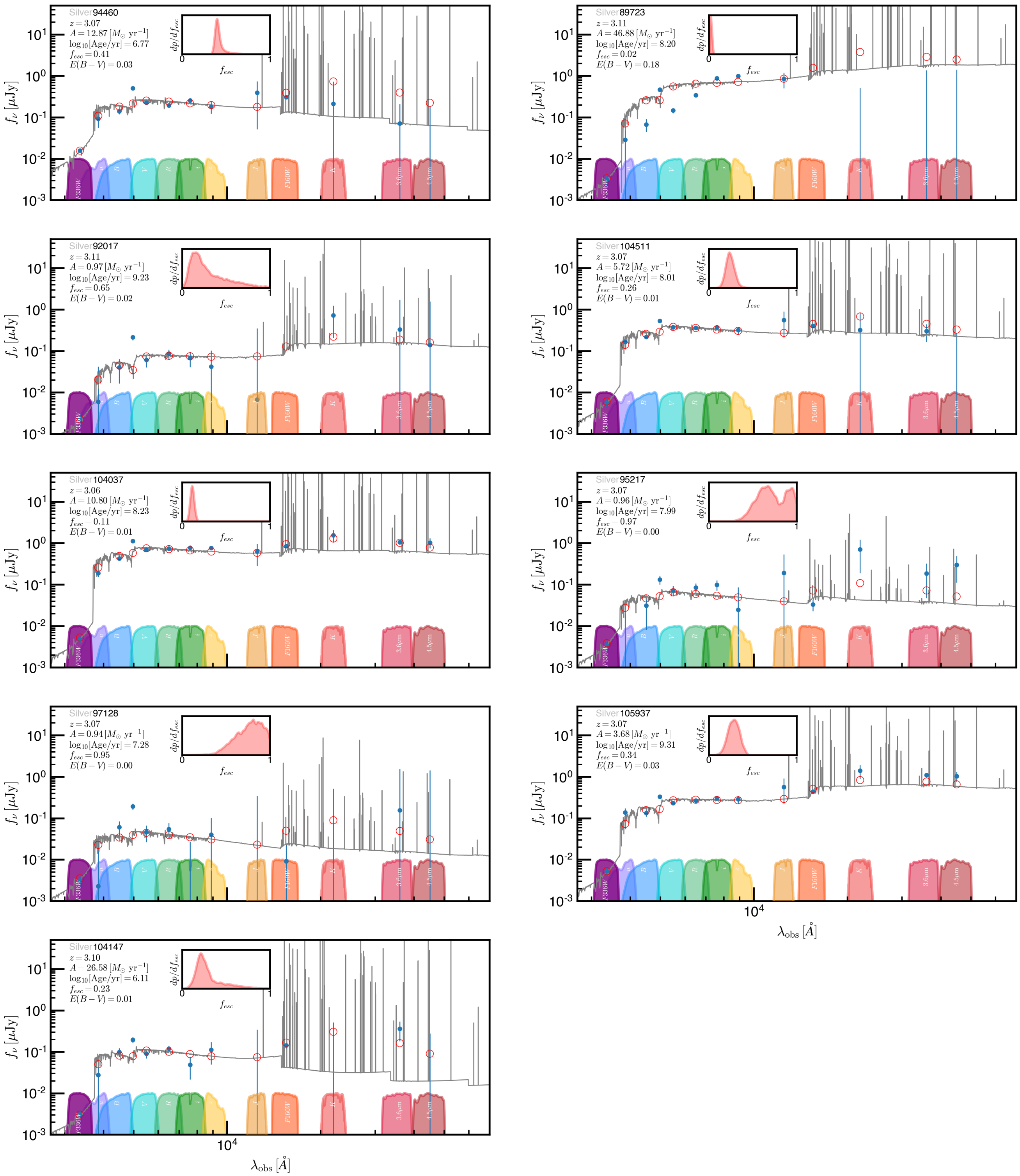

FIG. 9.— SED fits to silver subsample $z \simeq 3.1$ LAEs. The photometric data (blue points with error bars) for each source across 12 bands (colored regions) is used to constrain the SED model fit (gray line), resulting in the model photometry (open red circles). The maximum likelihood parameters for the star formation rate, the age of the constant star formation rate stellar population, the extinction, and the Lyman continuum escape fraction are reported. The insets show the marginal constraint on the escape fraction f_{esc} for each object.

TABLE 5
SED Parameter Constraints

ID	$A_{\rm SFR}$ [$M_\odot$/yr^{-1}]	$t_{\rm age}$ [$\log_{10}$ yr]	$M_\star$ [$\log_{10} M_\odot$]	$E(B-V)$	$f_{\rm esc}$	$\tilde{f}_{\rm esc,rel}$
Gold Sample						
86861*	9.18 ± 0.41	8.44 ± 0.10	9.41 ± 0.08	< 0.01	0.43 ± 0.04	0.22 ± 0.02
90675	9.04 ± 8.18	6.87 ± 0.87	7.63 ± 0.55	0.05 ± 0.03	0.52 ± 0.22	1.30 ± 0.76
92616	25.41 ± 14.10	6.42 ± 0.33	7.74 ± 0.15	0.03 ± 0.02	0.64 ± 0.33	1.44 ± 0.24
93564	72.86 ± 63.59	6.90 ± 0.32	8.67 ± 0.14	0.06 ± 0.01	0.50 ± 0.07	0.22 ± 0.03
90340	4.23 ± 0.94	8.21 ± 0.39	8.83 ± 0.30	0.03 ± 0.01	0.57 ± 0.13	0.46 ± 0.07
100871	6.40 ± 6.14	6.95 ± 0.78	7.56 ± 0.45	0.03 ± 0.02	0.50 ± 0.20	0.74 ± 0.30
103371	5.02 ± 3.55	6.59 ± 0.43	7.17 ± 0.18	0.02 ± 0.02	0.82 ± 0.11	0.90 ± 0.39
84986	18.64 ± 9.36	6.48 ± 0.56	7.66 ± 0.31	0.03 ± 0.01	0.33 ± 0.10	0.89 ± 0.28
92863	5.59 ± 4.43	8.29 ± 0.64	8.99 ± 0.48	0.07 ± 0.02	0.27 ± 0.11	0.36 ± 0.10
Silver Sample						
94460	27.89 ± 20.11	6.67 ± 0.49	7.99 ± 0.23	0.03 ± 0.01	0.42 ± 0.07	1.04 ± 0.13
89723	43.74 ± 5.49	8.29 ± 0.18	9.93 ± 0.14	0.17 ± 0.01	0.02 ± 0.01	0.12 ± 0.04
92017	9.66 ± 11.37	7.24 ± 1.01	7.94 ± 0.61	0.05 ± 0.03	0.30 ± 0.20	0.35 ± 0.15
104511	6.12 ± 0.85	7.89 ± 0.26	8.67 ± 0.21	0.01 ± 0.01	0.24 ± 0.05	0.20 ± 0.04
104037	11.01 ± 1.04	8.20 ± 0.15	9.24 ± 0.11	0.01 ± 0.01	0.12 ± 0.02	0.08 ± 0.02
95217	2.09 ± 2.36	7.43 ± 0.59	7.63 ± 0.36	0.02 ± 0.01	0.72 ± 0.17	0.51 ± 0.20
97128	3.93 ± 2.94	6.68 ± 0.60	7.12 ± 0.28	0.02 ± 0.02	0.76 ± 0.15	0.74 ± 0.39
105937	4.71 ± 1.38	8.99 ± 0.28	9.65 ± 0.21	0.04 ± 0.01	0.28 ± 0.06	0.25 ± 0.05
104147	9.92 ± 8.77	7.08 ± 0.96	7.87 ± 0.57	0.02 ± 0.01	0.30 ± 0.16	0.33 ± 0.11
Composite SEDs						
Gold	28.16 ± 15.87	6.44 ± 0.22	7.82 ± 0.05	0.05 ± 0.01	0.22 ± 0.03	0.65 ± 0.11
Silver	6.13 ± 0.62	8.16 ± 0.16	8.95 ± 0.13	0.06 ± 0.01	0.21 ± 0.05	0.31 ± 0.06
Non-Detections	1.89 ± 0.48	8.33 ± 0.43	8.59 ± 0.32	0.05 ± 0.01	0.003 ± 0.04	< 0.05

band centroid for each of the LACES LAEs, for all of the available photometric bands. The composites were generated by stacking these cutout images for each band for the gold, silver and non-detected subsamples using the IRAF task `imcombine`. Only LAEs within the SSA22 protocluster at approximately $z \simeq 3.1$ were included and LAEs with $z > 3.1$, such as ID 93564 were excluded from the composites.

The errors for the composite SEDs were calculated by first masking all objects with SNR > 3 in each image. Regions were then selected from the remaining noise, ensuring no overlap with masked areas of the image. These regions were then used to make stacked images of the noise, stacking the same number of images used in the gold, silver and non-detection composites (N $= 8, 9, 32$ respectively). This process was repeated across every photometric band for 500 stacks of the noisy regions and the 1σ upper limits were calculated.

Table 6 provides the flux density and associated 1σ uncertainty measured in each band for the composite stacks for our gold, silver, and non-detection subsamples. Using the higher-precision composite SEDs, we again perform our SED model fits to explore possible inferred differences between the composite properties of our subsamples.

TABLE 6
Composite SEDs

Band	Gold Sample Flux [nJy]	Silver Sample Flux [nJy]	Non-detection Sample Flux [nJy]
F336W	7.12 ± 1.21	4.86 ± 1.00	< 0.27
U	63.7 ± 6.6	48.3 ± 10.4	9.91 ± 5.58
B	77.3 ± 4.6	101.9 ± 7.9	34.4 ± 3.9
NB497	457.1 ± 5.2	346.8 ± 9.1	207.0 ± 4.7
V	138.1 ± 6.1	173.8 ± 6.0	70.5 ± 3.4
R	147.2 ± 7.2	205.1 ± 6.8	68.6 ± 3.5
I	150.0 ± 4.8	270.4 ± 8.0	89.5 ± 4.2
Z	123.6 ± 9.5	319.2 ± 16.4	78.7 ± 8.4
J	158.5 ± 76.4	369.9 ± 118.8	127.1 ± 63.5
F160W	304.8 ± 12.7	331.2 ± 13.8	139.3 ± 6.9
K	40.6 ± 94.4	398.1 ± 181.5	169.1 ± 105.4
[$3.6\mu m$]	291.1 ± 82.6	515.3 ± 180.7	195.9 ± 61.5
[$4.5\mu m$]	59.2 ± 118.3	87.1 ± 271.0	178.7 ± 110.9

4.4.1. *Gold Subsample Composite SED*

Figure 10 shows the maximum likelihood model fit to the stacked photometry of the gold sample. This composite at $z \approx 3.1$ appears to be consistent with a very young star-forming population, a reddening of $E(B-V) \approx 0.05$, and an escape fraction of $f_{\rm esc} \approx 0.2$. This SED-inferred escape fraction is lower than the relative escape fraction suggested by ratio of the 900 Å and 1500 Å rest-frame flux densities and the typical $f_{\rm esc}$ suggested by the individual gold subsample object fits. This discrepancy results from improved constraints on the rest-frame UV portion of the spectrum gained by stacking. Compared to the other composites discussed below, the mean age is younger although less certain. This reflects the wider range of inferred ages in the individual objects in the gold sample as listed in Table 5. If the mean age were increased, making it more consistent with that for the other composites, the inferred escape fraction for the gold

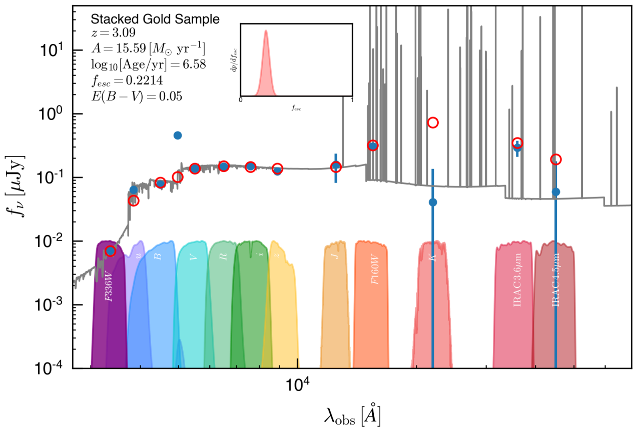

FIG. 10.— SED model fit to photometry of stacked gold sample detections.

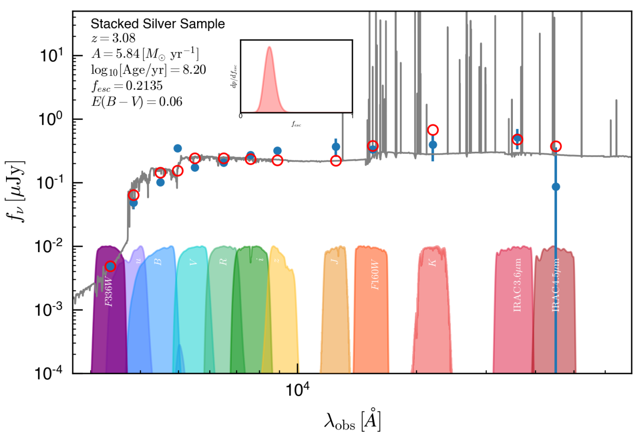

FIG. 11.— SED model fit to photometry of stacked silver sample detections.

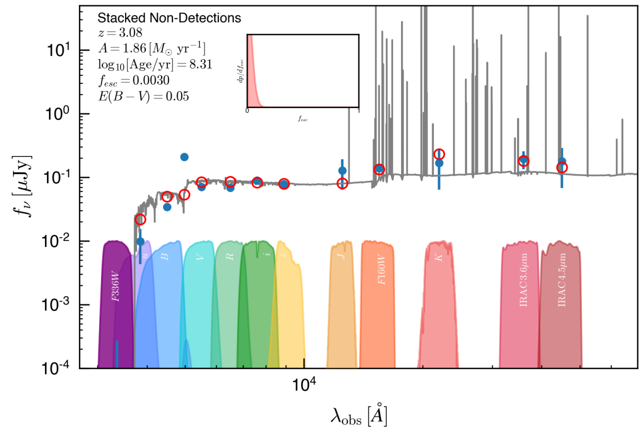

FIG. 12.— SED model fit to photometry of stacked non-detections.

sample would be larger.

4.4.2. *Silver Subsample Composite SED*

Figure 11 shows the maximum likelihood model fit to the stacked photometry of the silver subsample. Relative to the gold subsample composite, the silver subsample composite at $z \approx 3.08$ is consistent with being older and forming stars at a lower rate, but with a comparable reddening $E(B-V) \approx 0.06$. The inferred silver composite escape fraction is the same as for the gold composite, with $f_{esc} \approx 0.2$.

4.4.3. *F336W Non-Detection Subsample Composite SED*

Figure 12 shows the maximum likelihood model fit to the stacked photometry of the *F336W* Non-Detection subsample. This composite at $z \sim 3.1$ is consistent with a 500 Myr-old stellar population forming stars at $A_{\rm SFR} \lesssim 2M_\odot$/yr, lightly reddened, and with a Lyman escape fraction close to zero (i.e., $f_{esc} < 0.003$). In our models, the low escape fraction results in strong nebular continuum and line emission in the rest-frame optical, and the model photometry agrees well with the stacked photometric data at these wavelengths.

5. RESULTS

We can now take full advantage of our large sample with individually determined $f_{\rm esc}$ values and investigate possible trends with other galaxy properties so we may better understand the mechanisms through which LyC photons escape.

5.1. *Dependence on the Strength of Lyα*

The mechanisms through which LyC and Lyα photons escape may be very similar if geometry plays a dominant role in the escape of ionizing photons. Low-density channels created by a burst of star-formation may enable LyC and Lyα photons to leak out in a specific direction. However, the radiative transfer of LyC and Lyα differ, which may influence their relative visibility. Lyα is absorbed by dust and is a resonant line and can thus be scattered back into the line of sight by neutral hydrogen, whereas LyC photons can only be absorbed by dust and neutral hydrogen. Therefore it may be possible to have significant Lyα escape whilst that of Lyman continuum photons is suppressed.

Contrary to this picture, extreme Lyα emission would imply that most of the ionizing photons have been reprocessed as Lyα photons, allowing few LyC photons to escape. However, Nakajima & Ouchi (2014) predict that significant $f_{\rm esc}$ and large $\rm EW_{Ly\alpha}$ are possible for $f_{\rm esc} < 0.8$ and it is only for very extreme escape fractions that Lyα will be suppressed.

Many authors have reported a positive correlation between the $\rm EW_{Ly\alpha}$ and escaping LyC photons. Verhamme et al. (2017) reported this empirical relation using the small number of confirmed LyC-leaking low-redshift sources. At intermediate redshifts the trend has also been observed using stacked spectroscopy (Marchi et al. 2017) and ground-based imaging (Micheva et al. 2017b), the latter of which may be affected by foreground-contamination.

For the LACES sample deep imaging in the Subaru narrow-band covering all our targets allows us to determine accurate estimates for the $\rm EW_{Ly\alpha}$. We use the Subaru photometry instead of our spectroscopic data because the extended Lyα flux can be included without slit losses and we can easily compare the flux measured in the narrow band to the continuum measured in the broad bands. We show our individually-determined escape fractions against $\rm EW_{Ly\alpha}$ in the top-left panel of Figure 13. There does appear to be a positive correlation albeit with large scatter. Uncertainty in the likelihood of $f_{\rm esc}$ arises

TABLE 7
Photometry of the LyC Leaking Candidates

ID	U	B	NB497	V	R	i'	z'	J	F160W	K	[3.6]	[4.5]	[5.8]	[8.0]
Gold Sample														
86861*	25.6	24.6	22.7	24.0	24.1	24.4	24.7	> 23.9	24.2	> 23.4	22.8	23.1	> 22.5	> 22.3
93564	> 26.3	25.8	25.3	24.9	24.7	24.3	24.3	> 23.9	24.6	22.9	> 22.4	> 22.3	–	–
90340	26.0	26.7	25.6	25.8	25.4	25.3	24.9	> 23.9	25.4	> 23.4	> 22.4	> 22.3	–	–
84986	> 26.3	> 26.8	25.9	26.7	26.6	26.6	> 25.7	> 23.9	25.8	> 23.4	> 24.8	> 24.5	> 22.5	> 22.3
92863	26.1	> 26.8	25.6	26.3	25.9	25.3	25.5	> 23.9	25.0	> 23.4	> 22.4	> 22.3	–	–
90675	> 26.3	> 26.8	25.9	> 26.9	> 26.9	> 26.6	> 25.7	> 23.9	25.4	> 23.4	> 22.4	> 22.3	–	–
92616	> 26.3	26.3	25.0	26.1	26.1	26.1	> 25.7	> 23.9	–	> 23.4	> 22.4	> 22.3	> 21.7	> 21.6
100871	> 26.3	> 26.8	25.6	> 26.9	> 26.9	> 26.6	> 25.7	> 23.9	–	> 23.4	> 24.8	> 24.1	> 22.5	> 21.6
103371	> 26.3	> 26.8	24.9	26.8	> 26.9	> 26.6	> 25.7	> 23.9	> 27.4	> 23.4	> 24.8	> 24.1	> 22.5	> 21.6
Silver Sample														
94460	> 26.3	26.0	24.5	25.5	25.6	25.4	> 25.7	> 23.9	25.1	> 23.4	> 24.8	> 24.5	> 22.5	> 22.3
104511	25.7	25.5	24.5	25.0	25.0	25.0	25.2	> 23.9	25.1	> 23.4	> 24.8	> 24.1	> 22.5	> 21.6
104037	25.5	24.8	23.7	24.2	24.2	24.2	24.1	> 23.9	24.0	> 23.4	23.5	23.4	> 22.5	> 21.6
105937	26.0	26.0	24.9	25.4	25.3	25.2	25.2	> 23.9	25.4	> 23.4	23.9	23.9	> 22.5	> 21.6
104147	> 26.3	26.2	25.5	26.3	26.0	> 26.6	> 25.7	> 23.9	26.1	> 23.4	> 24.6	> 24.1	> 21.7	> 21.6
89723	> 26.3	> 26.8	24.7	26.0	25.1	24.1	23.9	> 23.9	–	> 23.4	> 22.4	> 22.3	–	–
92017	> 26.3	> 26.8	25.6	> 26.9	26.6	> 26.6	> 25.7	> 23.9	–	> 23.4	> 22.4	> 22.3	> 21.7	–
95217	> 26.3	> 26.8	25.8	26.9	26.6	26.4	> 25.7	> 23.9	27.1	> 23.4	24.3	24.4	> 22.5	> 22.3
97128	> 26.3	> 26.8	25.7	> 26.9	> 26.9	> 26.6	> 25.7	> 23.9	> 27.4	> 23.4	> 22.4	> 22.3	–	–
Other Candidates														
107585	> 26.3	26.7	25.8	26.4	26.2	26.1	> 25.7	> 23.9	–	> 23.4	24.7	> 24.1	> 22.5	> 21.6
89114	> 26.3	26.3	25.1	26.1	25.9	25.8	> 25.7	> 23.9	26.8	> 23.4	> 24.8	> 24.5	> 22.5	> 22.3
106500	> 26.3	> 26.8	25.5	26.3	26.3	26.2	> 25.7	> 23.9	26.6	> 23.4	22.4	22.1	22.1	> 21.6

due to degeneracies in choosing slightly different models to fit the SED of each galaxy. It should be noted previous work exploring this correlation at intermediate redshifts did not include such model-dependencies as the observed flux density ratio of LyC to rest-frame UV photons was used instead of $f_{\rm esc}$.

We also calculate the escape fraction of Lyα ($f_{\rm esc}^{\rm Ly\alpha}$) by taking the ratio of the observed Lyα flux to the predicted intrinsic Lyα flux derived from the observed Hβ flux using recombination physics,

$$f_{\rm esc}^{\rm Ly\alpha} = \frac{F({\rm Ly\alpha})}{8.7 \times 2.86 \times F({\rm H\beta})}, \quad (3)$$

where we use the ratios Lyα/Hα = 8.7 and Hα/Hβ = 2.86 (Hayes 2015).

A positive correlation between $f_{\rm esc}^{\rm LyC}$ and $f_{\rm esc}^{\rm Ly\alpha}$ has been reported for the small number of low-redshift LyC leaking galaxies (Verhamme et al. 2017). The fact that Lyα appears to escape preferentially to LyC may imply LyC escapes through channels in a 'riddled ionization-bounded nebula' (Zackrisson et al. 2013; Behrens et al. 2014; Verhamme et al. 2015), whereas Lyα can escape additionally due to resonant scattering. Radiative transfer simulations (Dijkstra et al. 2016) reproduce these trends albeit with much scatter for $f_{\rm esc}^{\rm Ly\alpha} > 0.1$ due to the effects of dust, outflow kinematics and covering factor. For the present sample, no clear correlation between $f_{\rm esc}^{\rm LyC}$ and $f_{\rm esc}^{\rm Ly\alpha}$ is seen, but uncertainties arising from our faint Hβ detections may mask a genuine trend.

At first sight, it is puzzling to find a relatively strong correlation between $f_{\rm esc}^{\rm LyC}$ and EW$_{\rm Ly\alpha}$ but not between $f_{\rm esc}^{\rm LyC}$ and $f_{\rm esc}^{\rm Ly\alpha}$ when EW$_{\rm Ly\alpha} \propto {\rm f}_{\rm esc}^{\rm Ly\alpha} \times (1 - {\rm f}_{\rm esc}^{\rm LyC}) \times \xi_{\rm ion}$. However, the $f_{\rm esc}^{\rm LyC}$-EW$_{\rm Ly\alpha}$ correlation may have a marginal dependence on M$_{\rm UV}$. UV-fainter LACES objects tend to have larger EW$_{\rm Ly\alpha}$, as seen for many samples in the literature (Stark et al. 2010; Schenker et al. 2012; Ono et al. 2012). This may be due in part to increased $\xi_{\rm ion}$ (Nakajima et al. 2018). In Section 5.2 we show that $f_{\rm esc}^{\rm LyC}$ is anti-correlated with UV luminosity and stellar mass. Therefore, it is not surprising that LAEs with the most extreme $f_{\rm esc}$ and EW$_{\rm Ly\alpha}$ are intrinsically faint in M$_{\rm UV}$. Thus $f_{\rm esc}$ correlates with EW$_{\rm Ly\alpha}$ because the fainter objects are more compact with a harder $\xi_{\rm ion}$ which boosts EW$_{\rm Ly\alpha}$.

5.2. *Dependence of $f_{\rm esc}$ on Luminosity and Stellar Mass*

Understanding the typical $\xi_{\rm ion}$, $f_{\rm esc}$ and M$_{\rm UV}$ of galaxies at $z > 6$ is crucial in determining whether galaxies were the primary driver of cosmic reionization. Current estimates assume an average $f_{\rm esc}$ and $\xi_{\rm ion}$ and extrapolate the UV luminosity function down to a limiting magnitude, fainter than current observations (Robertson et al. 2013). It has been suggested that fainter galaxies may have higher $f_{\rm esc}$ or $\xi_{\rm ion}$, contributing enough ionizing photons such that galaxies alone are capable of reionizing the universe (e.g., Inoue et al. 2006; Kuhlen & Faucher-Giguère 2012; Bouwens et al. 2012; Finkelstein et al. 2012; Fontanot et al. 2012, 2014; Robertson et al. 2013; Faisst 2016).

In Nakajima et al. (2018) we have already shown for a similar sample of LAEs in the SSA22 protocluster that the production efficiency of ionizing photons, $\xi_{\rm ion}$, increases towards lower UV luminosities. We now explore whether $f_{\rm esc}$ also increases at fainter luminosities in our LACES sample. The top-right plot in Figure 13 shows the correlation between M$_{\rm UV}$ and $f_{\rm esc}$ for the individual objects in the LACES gold and silver samples. There appears to be a correlation such that LAEs with fainter UV luminosities have larger $f_{\rm esc}$. Grazian et al. (2017) found

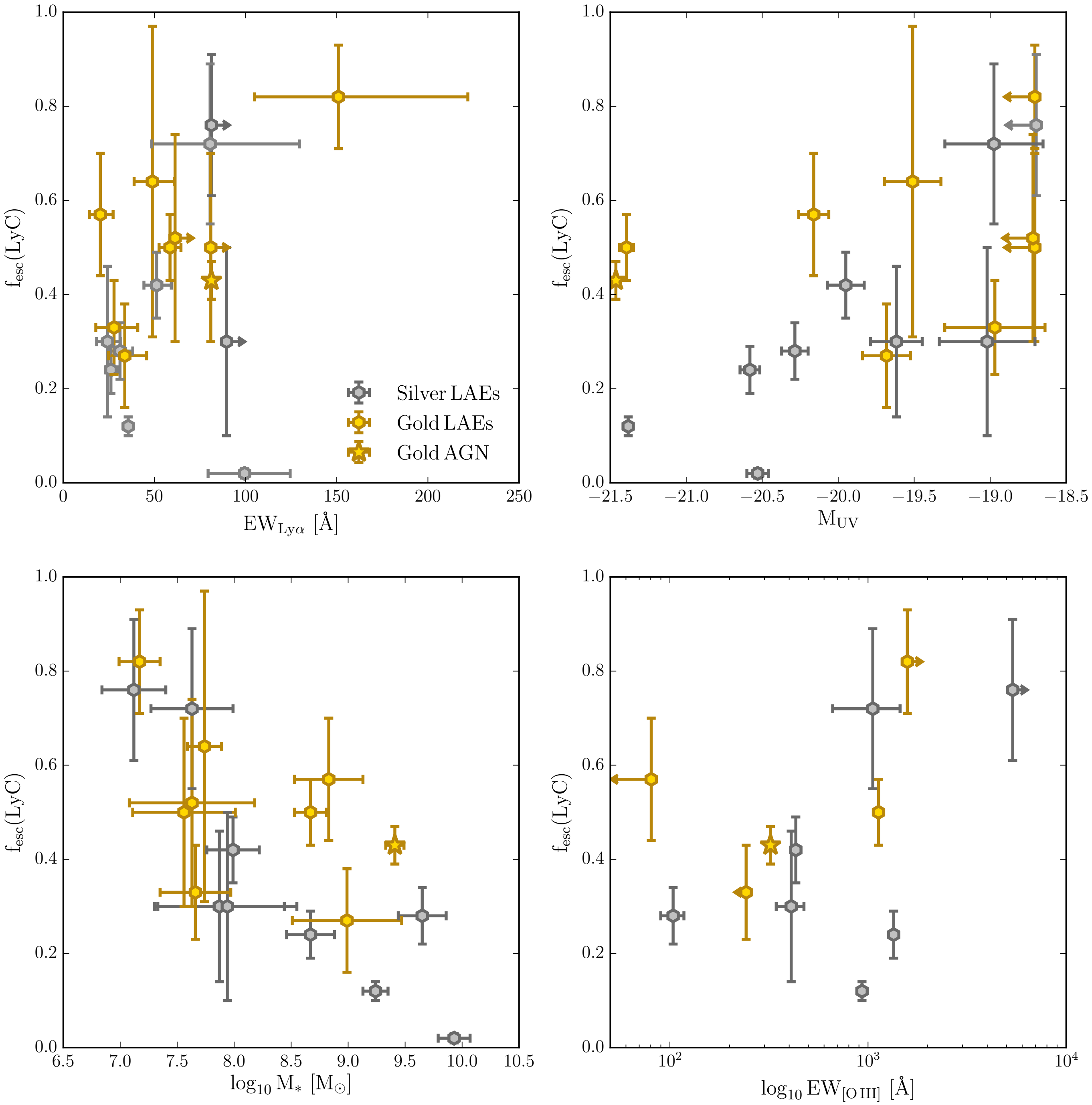

FIG. 13.— Correlations between f_{esc} and other observed and derived properties for the LACES gold and silver samples. Top-left: dependence of f_{esc} on $EW_{Ly\alpha}$. Top-right: dependence of f_{esc} on UV luminosity. Bottom-left: dependence of f_{esc} on stellar mass. Bottom-right: Dependence of f_{esc} on the equivalent width of [O III]. In the bottom-left panel both f_{esc} and stellar mass are inferred model-dependent parameters where the stellar mass is the product of the age and SFR derived from SED fitting. Indeed, at fixed age it is expected that the SFR and f_{esc} would covary to match the *F336W* measurements and could produce this trend.

tentative evidence suggesting this trend using mostly limits on $f_{esc,rel}$ derived from ground-based imaging. However, all but 3 of their points were upper limits for $f_{esc,rel}$, therefore this result may simply be due to the U-band imaging depth of their observations. All the LACES objects presented here are detected LyC leakers. There are a few outliers at the bright end of our sample for which $f_{esc} \sim 0.5$ although one of these is an AGN (denoted by the gold star).

It has been suggested that this correlation could be due only to the fact that galaxies with a lower luminosity will tend to also be lower mass and there is an anti-correlation between stellar mass and the O_{32} ratio (Nakajima & Ouchi 2014; Faisst 2016; Dijkstra et al. 2016) which itself is expected to correlate with f_{esc} (Jaskot & Oey 2013; Nakajima & Ouchi 2014; Nakajima et al. 2016; Faisst 2016; Izotov et al. 2018). Indeed, in the bottom-left panel of Figure 13 we see that the stellar mass is anti-correlated with $f_{\rm esc}$ for the same objects. It must be noted that this Figure plots two SED-derived parameters, both of which are model-dependent.

To summarize, we find that lower-mass, intrinsically fainter galaxies appear to have larger escape fractions. There are two possible explanations.

If geometry plays a significant role, less massive galaxies with shallow gravitational potential wells will be more susceptible to bursts of star formation creating holes in the ISM, allowing LyC photons to escape. This scenario can be thought of as a 'riddled ionization bounded nebula', and because LyC photons only escape through a small channel the O_{32} ratio does not need to be extreme.

Alternatively these lower-mass LAEs may be more efficient at converting gas into stars, with a higher specific star formation rate and shorter depletion time. Therefore, these galaxies will have more ionizing photons per atom and their ISM will be more readily ionized, as in the density-bounded hypothesis (Nakajima & Ouchi 2014). LyC photons can then escape in all directions and this will result in an enhanced O_{32} ratio.

5.3. *Dependence of $f_{\rm esc}$ on the Strength of [O III]*

There is growing evidence that the O_{32} ratio correlates with $f_{\rm esc}$ (Nakajima & Ouchi 2014; Nakajima et al. 2016; Faisst 2016; Izotov et al. 2018). Characterizing the mean $f_{\rm esc}$ of $z \sim 3.1$ LAEs with extreme O_{32} will be useful in understanding the role similar $z > 6$ LAEs, where LyC emission is not directly observable due to a partially neutral IGM, have in contributing to reionization. Unfortunately, due to observational constraints, we did not obtain deep enough [O II] measurements to properly correlate O_{32} with $f_{\rm esc}$ for a statistically meaningful sample.

In the absence of [O II] measurements we instead use the equivalent width of [O III] as a large $\rm EW_{[O\,III]}$ may imply a large O_{32} ratio. This appears to be a reasonable assumption and (Tang et al. 2018, in prep.) find that galaxies with large $\rm EW_{[O\,III]}$ almost always have large O_{32}. Moreover, it appears that galaxies in the reionization-era differ in that they have more extreme [O III] as the strength of the [O III] line appears to increase with redshift (Schenker et al. 2013; Smit et al. 2014, 2015). The discovery that LBGs at $z > 7$ with extreme [O III] have been detected with Lyα emission also implies a large $f_{\rm esc}$ as these objects may have ionized bubbles of hydrogen early so that their Lyα emission could redshift out of resonance with neutral hydrogen and escape (Roberts-Borsani et al. 2016; Zitrin et al. 2015; Oesch et al. 2015; Laporte et al. 2017; Stark et al. 2017).

We use the equivalent width instead of the flux, as our objects span a wide range of magnitudes. Therefore, in order to accurately calculate the $\rm EW_{[O\,III]}$ we require that our LAEs were targeted and detected in our MOSFIRE campaign but also that our targets were covered by the deep HST *F160W* photometry so we can accurately estimate the continuum at the [O III] line (see section 2.3).

We show the results for the LACES sample in the bottom-right panel of Figure 13. There is a tentative positive correlation between $\rm EW_{[O\,III]}$ and $f_{\rm esc}$ again with large scatter, suggesting that a larger $\rm EW_{[O\,III]}$ does imply a larger $f_{\rm esc}$. However, we cannot test the physically-motivated hypothesis that density-bounded nebulae result in LyC leakage. Indeed ionization-bounded nebulae can have the same size O^{++} zone as density-bounded nebulae and not be leaking LyC. Nevertheless, this result shows that extreme $\rm EW_{[O\,III]}$ emission correlates with large escape fractions. With $\rm EW_{[O\,III]}$ likely correlating with O_{32} (Tang et al. 2018, in prep.) we can infer there may be a tentative trend between $f_{\rm esc}$ and O_{32}. Further [O II] measurements would enable us to correlate $f_{\rm esc}$ directly with O_{32} for the LACES gold and silver subsamples.

6. DISCUSSION

The robust detection of Lyman continuum photons from a substantial subset of our LAE sample, combined with stringent limits on Lyman continuum escape in our non-detected objects, may provide clues as to how galaxies physically release hydrogen ionizing photons as required if they drove cosmic reionization. Below, we examine possible differences between our detected and non-detected samples, discuss possible physical mechanisms for the escape of Lyman continuum photons that may explain our results, and compare with previous searches for Lyman continuum emission in galaxies.

6.1. *Understanding the Non-Detections*

We now discuss the puzzling dichotomy between our LyC detections and non-detections. The 18 LyC-leaking LAEs are all individually detected with SNR > 3 in the *F336W* images and have $f_{\rm esc} \sim 2 - 82\%$, whereas even in a mean composite spectrum of 32 non-detections we estimate $f_{\rm esc} < 0.3\%$.

We first investigate whether there are any differences between these two populations in terms of their luminosity ($\rm M_{UV}$), strength of Lyα emission ($\rm EW_{Ly\alpha}$), $\rm EW_{[O\,III]}$ and velocity offset of Lyα ($\Delta v_{\rm Ly\alpha}$). In Figure 14 we show how the detections, including gold, silver and other candidates ($N = 21$) and the non-detections ($N = 32$) are distributed across these parameters with reference to the full sample of 53 LAEs. It appears that the population of detections and non-detections are almost indistinguishable from one another. LyC-detected objects span the full range of UV luminosities as do the non-detections. However, it should be noted that there is an observational bias at fainter luminosities as we will not be able to detect small escape fractions in individual cases for the faintest LAEs. Indeed, we saw in Section 5.2 that $f_{\rm esc}$ increases for fainter LAEs with increasing scatter so it remains possible that some of the faint LAEs in the LyC non-detections are weak to moderate LyC-leakers but below our detection limit. Nevertheless, if this were the case we would still expect to detect this faint signal in the deep *F336W* stack, yet we recover on average $f_{\rm esc} < 0.3\%$.

Additionally, LyC-detected LAEs have a similar distribution in $\rm EW_{Ly\alpha}$ with respect to non-detections. However, our LyC detections are almost all at $\rm EW_{Ly\alpha} <$ 100 Å, as is the case for most of the LAEs in the LACES sample. Of the 6 LAEs with $\rm EW_{Ly\alpha} > 100$ Å only 1 is a LyC leaker. This trend may be expected if LAEs with very large $\rm EW_{Ly\alpha}$ have reprocessed almost all of their ionizing photons into Lyα, resulting in galaxies with $f_{\rm esc} \sim 0$ (e.g., Nakajima & Ouchi 2014). These LAEs are also the faintest objects discussed above, so even if they have a non-zero $f_{\rm esc}$ it will most likely be below our detection limit. Regardless, the bulk of the non-leaking LAEs contributing to the composite spectrum have moderate $EW_{Ly\alpha}$ and M_{UV} and fall in the same space in a $EW_{Ly\alpha}$-M_{UV} plot as the bulk of the detections. Therefore, given the evidence from the detections (Section 5.1 and 5.2) we would have expected these LyC non-detections to have moderate f_{esc} that would be detectable in our deep $F336W$ stack. Yet, we detect no signal when stacking these objects and find $f_{esc} < 0.3\%$. This could be due to differences in the covering factor of these LAEs, however we do not probe this property in our observations.

We also examine the distribution of $EW_{[O\,III]}$ in Figure 14. Once again, the detections cover the full range of $EW_{[O\,III]}$ as do the non- detections except for one of the LyC detections which has $EW_{[O\,III]} > 5372$Å. If LyC leakage arises due to density-bound nebulae with extreme O_{32} ratios this may imply extreme $EW_{[O\,III]}$ (Tang et al. 2018, in prep.). We would therefore expect the LyC detections to be preferentially clustered at large $EW_{[O\,III]}$ compared to the non-detections. However, the majority of the detections fall at $EW_{[O\,III]} \lesssim 2000$Å with a few objects having extreme $EW_{[O\,III]}$. Again, it may be the case that if galaxies are leaking a significant fraction of their ionizing photons there are few > 35 eV photons remaining to doubly ionize oxygen. This could perhaps explain why some of our LyC leakers have smaller $EW_{[O\,III]}$. It is important to note that $EW_{[O\,III]}$ measurements have not been obtained for all the LAEs as [O III] was not targeted or detected for every object and we do not have full $F160W$ coverage for the LACES sample in order to estimate the continuum at ~ 5000 Å in the rest-frame.

Finally we examine the distributions of $\Delta v_{Ly\alpha}$, which should be $< 150\,\mathrm{km\,s^{-1}}$ for LyC leakers that require a low column density of neutral gas for LyC escape (Verhamme et al. 2015). We find no significant difference between detections and non-detections. We will discuss this result in more detail below in Section 6.1.1.

To summarize $\sim$ 33% of the LAEs in the LACES sample have individual detections ranging from 2% to 82%. Using composite SEDs we find the average $f_{esc} = 0.22 \pm 0.03\%$ and $f_{esc} = 0.21 \pm 0.05\%$ for the gold and silver samples respectively. Even when using a stack of 32 LAEs that are not detected as LyC-leakers in individual $F336W$ images we find on average $f_{esc} < 0.3\%$ despite these LAEs having an almost identical distribution of luminosities, $EW_{Ly\alpha}$, $EW_{[O\,III]}$ and $\Delta v_{Ly\alpha}$ as the LyC-leakers. We now turn to possible explanations for this dichotomy.

6.1.1. *Anisotropic LyC Escape*

Previous analyses have proposed (Zackrisson et al. 2013; Behrens et al. 2014; Nakajima & Ouchi 2014) that there exist at least two mechanisms through which LyC photons can escape. The first involves an ionization-bounded nebula where H II and H I shells surround the central stars. LyC photons can escape from such a system if stellar winds or supernovae from a burst of star-formation produce low-density holes through the neutral hydrogen in the ISM. LyC photons can then easily escape through these channels without being absorbed. Alternatively if the stellar population has a very hard spectrum or there is a significant burst of star-formation, the resulting ionization of the gas may enable LyC photons to readily escape in all directions (Zackrisson et al. 2013; Behrens et al. 2014; Nakajima & Ouchi 2014).

If LAEs are ionization-bound with holes then it will only be possible to detect LyC leakage if our line of sight is coincident with the opening angle of these channels. All LAEs in a given sample could be leaking LyC radiation but only a fraction of them, corresponding to the average covering fraction of H I and dust, would be detected as LyC leakers through direct observations. The angular dependence of the escape fraction is found to be highly anisotropic in simulations, with galaxies with smaller f_{esc} having a smaller solid angle through which LyC photons can escape (Paardekooper et al. 2015). Therefore, if the escape of LyC photons occurs anisotropically through channels, it seems likely that our non-detections would have small f_{esc}, with the photons escaping out of small channels directed away from our line of sight. However, we do not probe the covering fraction of our LAEs and we cannot be certain that geometric effects are the main cause for the dichotomy between our detections and non-detections.

Using Lyα transfer calculations in H I regions, Verhamme et al. (2015) showed that if LyC escapes due to an optically thin ($N_{HI} \leq 10^{18}\,\mathrm{cm^{-2}}$), density-bounded regime then the Lyα profile will be narrow with a small velocity offset ($\Delta v_{Ly\alpha} < 150\,\mathrm{km\,s^{-1}}$). However, if the LyC-leakers are ionization-bounded and riddled with low-density channels $\Delta v_{Ly\alpha} \sim 0\,\mathrm{km\,s^{-1}}$ with a small red peak due to additional scattered Lyα light that then escapes through the channel. If the dichotomy between our detections and non-detections is caused by geometry we might expect the LyC-leakers to be preferentially clustered around $\Delta v_{Ly\alpha} \sim 0\,\mathrm{km\,s^{-1}}$ when compared to the non-detections.

In Figure 14 we show the distribution of $\Delta v_{Ly\alpha}$ for the detections and non-detections where both a Lyα and systemic redshift are available. The LyC detections cover the full range of velocity offsets and are not centered only around small velocity offsets. Therefore it is not clear that the non-detections are ionization-bounded whereas detections are riddled or density-bounded. Indeed, the Lyα profile is most likely more complex than this simple picture. Velocity offsets could be caused by outflows. Also, if LyC escapes through small offset channels, this geometry could have little implication for the Lyα profile, which may still be dominated by resonant scattering. More detailed analysis of Lyα spectra at higher spectral resolution are most likely needed before ruling out the geometric picture of Lyα escape.

6.1.2. *Stochastic LyC Escape*

Star formation at these redshifts may be highly time-dependent. Galaxies accrete gas from the IGM and through mergers. They undergo bursts of star-formation, as a result of which feedback in the form of stellar winds and supernovae can ionize their ISM. During the relatively quiescent periods, the ionized gas will recombine. LyC leakage may therefore be stochastic with bursts of star-formation either ionizing all the neutral hydrogen within the virial radius creating channels through which LyC photons can escape. This has been widely reported in simulations of leaking LyC radiation where f_{esc} has traced bursty star formation with a time delay of ~ 10

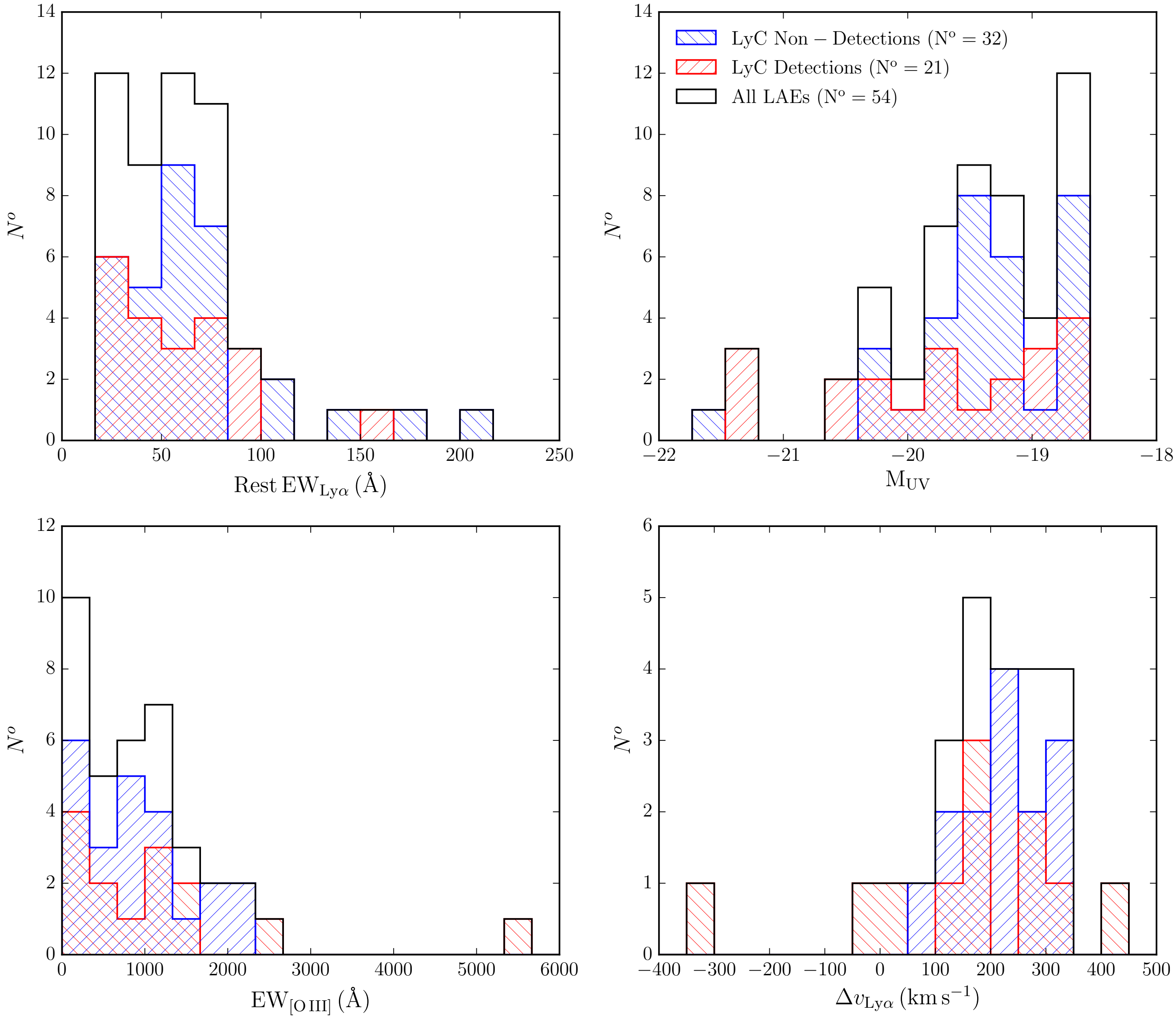

Fig. 14.— Distributions of $\mathrm{EW}_{\mathrm{Ly}\alpha}$ (top-left), M_{UV} (top-right), $\mathrm{EW}_{[\mathrm{O\,III}]}$ (bottom-left) and $\Delta v_{\mathrm{Ly}\alpha}$ (bottom-right) for the LACES sample. Red hatched histograms show the numbers of LAEs with detected $F336W$ emission and blue histograms show non-detected LAEs. The black outline shows the total number of LAEs in the detections and non-detections. The [O III] line and both a Lyα and systemic redshift were not always targeted or detected in our extensive optical and near-infrared spectroscopy. Therefore, in the two lower panels showing the distributions of $\mathrm{EW}_{[\mathrm{O\,III}]}$ and $\Delta v_{\mathrm{Ly}\alpha}$ we only show LAEs for which the relevant data is complete.

Myr (Kimm & Cen 2013; Wise et al. 2014; Ma et al. 2016; Kimm et al. 2017; Trebitsch et al. 2017) and with smaller, lower mass galaxies expected to be more stochastic.

We would therefore expect that the LACES LAEs with no leaking LyC radiation are being observed in these quiescent periods where the ISM has had time to recombine. However, this picture is difficult to reconcile due to large $\mathrm{EW}_{[\mathrm{O\,III}]}$ we observe for the non-detections, implying very recent star-formation. These galaxies may be recently star-forming but feedback may not have been effective in creating pathways for the radiation to escape. This ineffectiveness may trace an additional factor such as the covering fraction which could be varying between individual galaxies. Thus, galaxies with lower covering fractions are more able to leak LyC, given the same burst of star-formation and feedback.

In this scenario, only a fraction of LAEs at any time would be at a point where they had recently undergone a burst of star-formation ~ 10 Myr ago and only these LAEs would be detectable as having a non-zero f_{esc}. If it were possible to observe these LAEs over hundreds of Myr perhaps we would see the LAEs flash "on" and "off" in LyC emission.

6.1.3. *Spatially Varying Intergalactic Medium*

As our study takes place within the SSA22 protocluster, a further possibility is that the IGM is spatially varying on scales of tens to a few hundred Mpc within our area of study and the field of view of the $F336W$ images. This density variation would result in LyC leakage from LAEs in regions with a higher column density of H I being more strongly absorbed and thus we would measure

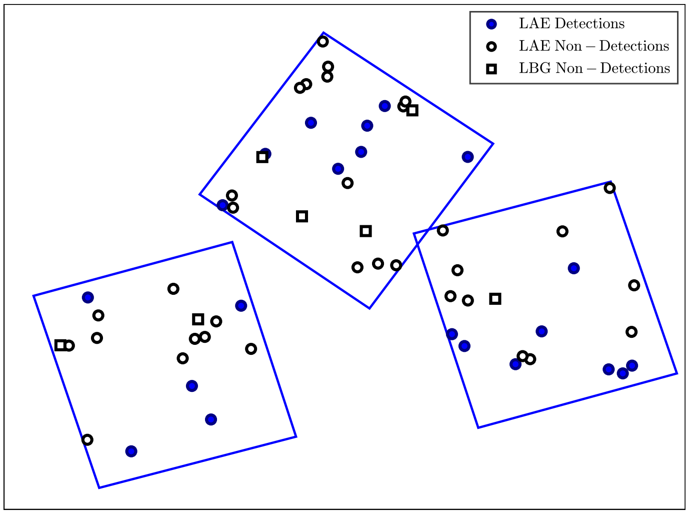

FIG. 15.— Spatial distribution of LyC detections (blue) and non-detections (white) for all LAEs and LBGs (circles and squares respectively) in the LACES sample. Detections and non-detections appear to be spatially clustered which could be due to spatial variations of H I gas in the SSA22 protocluster.

a reduced or zero $f_{\rm esc}$ for these objects.

Evidence for spatial variation of H I in the IGM and CGM within the SSA22 protocluster has been investigated in the literature. Using bright galaxies behind the protocluster, Mawatari et al. (2017) measured Lyα absorption in the spectrum of these galaxies due to absorption by H I within SSA22. They found that SSA22 has an excess of H I compared to similar independent control fields. They also found that there is a large scale diffuse H I component which is independent of the CGM of individual galaxies, Lyα absorption increased on < 100 Mpc scales possibly due to the CGM of nearby galaxies and that stronger LAEs had weaker H I absorption.

Mawatari et al. (2017) focused on the center of SSA22 and the LACES sample is drawn from the edge of the region considered in their study. It is therefore possible that there is large scale diffuse H I unconnected to individual LAEs within our field and that a particularly dense CGM of a nearby galaxy or an ionizing neighbor with a large $f_{\rm esc}$ may respectively inhibit or boost the chances of leaking LyC radiation reaching us as observers. Figure 15 shows the spatial distribution of LAE-LyC detections (blue circles) and LyC-non-detections for LAEs and LBGs (white circles and squares respectively).

Indeed, it does seem that the LyC detections and non-detections appear clustered on small scales which could be due to spatially varying H I in the IGM and CGM. We cannot directly measure the H I in the LACES field but future detections of leaking LyC radiation in clusters with lower H I density or in blank fields may help us understand if LyC non-detections in extreme LAEs owes to H I absorption. It should be noted that this effect would only change the fraction of leaking LyC radiation that is absorbed along the line of sight. We have still detected LyC escape in a significant fraction of our LAEs but it is possible more IGM absorption results in non-detections for the remaining LAEs.

6.2. *Comparison to Other Studies*

Through the LACES program, we have provided a significant number of individual LyC measurements for a homogeneous sample of star-forming galaxies in a narrow redshift interval at $z \simeq 3.1$, corresponding to escape fractions of $f_{\rm esc} \simeq 2 - 82\%$. Of particular significance is the high success rate ($\simeq 30\%$) within our sample, one considered to be potential analogs of [O III]-strong metal-poor sources in the reionization era.

Early efforts to directly measure significant escape fractions in galaxies at intermediate redshifts have largely been unproductive apart from a few exceptional cases (Shapley et al. 2016; de Barros et al. 2016; Vanzella et al. 2016; Bian et al. 2017; Vanzella et al. 2018). Without a sizable number of detections drawn from a homogeneous sample, it has therefore been difficult to make progress in understanding under what conditions LyC photons can escape.

An alternative approach when no individual detections can be found, for example due to the limited sensitivity of the data, is to stack the LyC signal from a large sample either with suitable photometry (Rutkowski et al. 2017; Matthee et al. 2017; Grazian et al. 2017; Japelj et al. 2017; Naidu et al. 2018) or spectroscopic data (Marchi et al. 2017; Steidel et al. 2018). However, with the exception of the recent campaign by Steidel et al. (2018), this has resulted primarily in upper limits of $f_{\rm esc} < 10\%$ below the canonical value of $10 - 20\%$ required to sustain reionization (Robertson et al. 2013). The results of these programs has led to speculation that reionization may not be driven by star-forming galaxies e.g. Madau & Haardt (2015).

An important conclusion from our work, which would not be easily seen in early stacking programs, is the distinction between the 18 LACES LAEs which show convincing individual detections in the range $f_{\rm esc} \simeq 2 - 82\%$ and 32 LAEs which, even when stacked, show no significant leakage consistent with an individual average $f_{\rm esc} < 0.3\%$. If, as we surmise, LyC leakage is either "on" or "off" due to anisotropic or time-varying factors, then *achieving adequate depth for an individual target is crucial to making the distinction.* If $z > 7$ sources had the same inferred escape fraction as our LyC detections, they could maintain reionization. Yet shallower surveys of sources less analogous to $z > 7$ objects would have concluded the opposite.

As an illustrative example, stacking $F275W$ photometry Rutkowski et al. (2017) found 1σ upper limits of $f_{\rm esc} < 14.0\%$ for 13 'extreme emission line galaxies' (EELGs) at $z \sim 2.3$ with $O_{32} > 5$. Although 3σ upper limits derived from their measurements could still be consistent with significant $f_{\rm esc}$ this result casts doubt on whether galaxies with extreme O_{32} are LyC leakers. Similarly Naidu et al. (2018) find $f_{\rm esc} < 16.7\%$ for fainter EELGs and $f_{\rm esc} < 8.5\%$ for their brighter EELGs using stacked ground-based U band imaging. However, if only a fraction of the LyC photons are escaping in our direction, then they will remain undetected in the relatively shallow images used by Rutkowski et al. (2017) (3σ depth ranging $26.5 - 28.2$ AB) whose depth was optimized for a composite stack.

The Steidel et al. (2018) spectroscopic campaign is the only comparative study which reaches a depth adequate for individual LyC detections comparable to escape fractions of $\simeq$10 percent. Individual detections were seen for 15/124 sources. The approach is highly complementary to the present study in several respects. It focuses on Lyman break galaxies (LBGs) over a wider redshift range with LyC signals inferred optimally from spectra in a narrow wavelength window (880-910 nm) where IGM absorption is reduced and samples multiple sightlines to reduce cosmic variance. The LACES program avoids some of the limitations of earlier HST imaging campaigns which targeted LBGs with a range of redshifts. LACES exploits a narrow-band selected sample of LAEs at $z \simeq 3.1$ optimally matched to the F336W filter and the improved depth of the HST imaging (a 3σ limiting magnitude of $\simeq 30.2$) to provide exquisite limits on individual sources with the necessary resolution to mitigate issues of foreground contamination.

Comparing the two approaches, the success rate of detecting LyC emission in the LACES sample (SNR ≥ 3 detections for 30% of the total sample and 33% for LAEs only) is higher than that seen for LBGs ($\simeq$10% to broadly comparable escape fractions in the Steidel et al. 2018 survey). Indeed, none of the 7 LBGs in our LACES control sample have detectable LyC emission. Our earlier work has shown LAEs have a harder $\xi_{\rm ion}$ than LBGs (Nakajima et al. 2016, 2018). With more ionizing photons, significant LyC leakage is more likely for LAEs and also results in larger O_{32} ratios and more extreme [O III] equivalent widths. LAEs can more readily leak LyC photons in riddled ionization-bounded or density-bounded nebulae, physical conditions more easily met for younger, low mass and metal-poor galaxies with important implications for comparable sources in the reionization era.

Despite the different approaches, many of the conclusions of the present paper are supported by the Steidel et al. (2018) results including the absence of any demographic differences between the sample of individual detections and those non-detected and similar correlations between $f_{\rm esc}$ and $\rm EW_{Ly\alpha}$ and $\rm M_{UV}$. The primary difference remains the higher success rate of detecting LyC leakages in LAEs and the possible association with [O III] emission.

6.3. *Implications for Cosmic Reionization*

Our interest in the LACES sample and this study is motivated, in part, by the likelihood that our $z \simeq 3.1$ LAEs are promising analogs of sources in the reionization era and thus that inferences on the physical conditions that permit LyC photons to escape will have important implications for the assumption that cosmic reionization is largely driven by similar systems.

It is reasonable to assume that LAEs at intermediate redshifts, that are metal-poor, low mass star-forming galaxies are similar to those at higher redshift. However, further simularities between our sample and typical $z > 7$ galaxies is based on meager data at high redshifts. These include promising indications that $z > 7$ galaxies have hard ionizing spectra (Stark et al. 2015, 2017; Laporte et al. 2017; Mainali et al. 2018) as seen in the LACES sample (Nakajima et al. 2016, 2018), as well as intense [O III] emission characteristic of many high redshift IRAC-excess sources (Smit et al. 2014, 2015; Roberts-Borsani et al. 2016). Assuming this is the case, what can be deduced from the fact that approximately $\simeq$ 33% of our LACES LAEs meet the canonical criterion for an escape fraction $f_{\rm esc} \geq 10\%$ required to drive reionization (Robertson et al. 2013, 2015)?

At face value, the *average* escape fraction for our LACES sample is substantially diminished by the dominant population for which no significant LyC leakage was detected to quite impressive limits. Nominally the average f_{esc} would be reduced from 20% (the mean of the gold and silver samples) to only 6% - a figure in reasonable agreement with the value determined for LBGs by Steidel et al. (2018).

However if, as seems possible, the dichotomy between our detections and non-detections is largely due to anisotropic LyC leakage, it is likely the majority of the LACES LAE are significantly influencing their local IGM. If a similar behavior is present in the reionization era, then such a coarse average would underestimate the role that early equivalents of the LACES population would play in governing reionization. Less luminous versions of our LAEs at high redshift could well have even higher escape fractions, as hinted by the trends in Figure 13. Additionally, the intrinsic fraction of LAEs is observed to increase with redshift (Stark et al. 2010; Schenker et al. 2012) and so we expect that an increasingly large fraction of high-redshift star-forming galaxies will look more and more like the LACES sample. Clearly, then, it is crucial to understand physically the dichotomy discussed in Section 6.1.

With this in mind, in later papers we will explore the dependence of f_{esc} on the ratio of [O III]/[O II] to test the density-bound concept first promoted by Nakajima & Ouchi (2014). The present MOSFIRE spectroscopic data has inadequate coverage of [O II] emission so such correlations cannot yet be examined. In addition, if the dichotomy discussed above originates via anisotropic LyC leakage, numerical simulations suggest that such high escape fractions may arise when feedback creates a turbulent interstellar gas enabling leakage through porous low density channels (Kimm & Cen 2013; Wise et al. 2014). This can be readily tested via IFU spectroscopy which aims to correlate our HST-determined escape fractions with spatially resolved ISM kinematics.

7. SUMMARY

We present the first results from the LymAn Continuum Escape Survey (LACES), where we obtained ultra-deep HST WFC3 UVIS/$F336W$ imaging of a sample of 61 faint $z \simeq 3.1$ LAEs and LBGs in the SSA22 field. The extreme depth of the $F336W$ images enabled individual direct detection of escaping Lyman continuum emission (SNR ≥ 3) in 18 LAEs (30%) in our homogeneous sample. Our program provides a huge increase in the number of individually detected LyC leakers at intermediate redshift and represents the first time a large sample of LAEs with a significant fraction of individual leakers has been presented. We make use of extensive multi-band photometry, including newly obtained HST WFC3 IR/$F160W$ imaging, to fit the SED of each galaxy to obtain accurate individual estimates of the escape fraction $f_{\rm esc}$. We further use our SED fitting method to infer typical escape fractions from composites of various subsamples. For individual objects we obtain $f_{\rm esc} \approx 2 - 82\%$ and for composites of our gold and silver subsamples of Lyman continuum detected objects we find $f_{\rm esc} \approx 20\%$. For our composite of the Lyman continuum non-detection subsample, we infer $f_{\rm esc} \lesssim 0.3\%$.

We expect the rate of contamination to be low (97% probability $\leq$ 3 of our detections could be contaminants) and we ensure against foreground interlopers using the high spatial resolution provided by the $F336W$ and $F160W$ images. We find that the escape fraction increases for lower mass, fainter galaxies with larger $EW_{Ly\alpha}$. LAEs with extreme $EW_{[O\,III]}$ also have more extreme f_{esc} which may suggest a correlation with O_{32}.

We discuss the dichotomy between our detections with significant f_{esc} and our non-detections, seemingly drawn from the same sample, covering the same range of UV luminosities, $EW_{Ly\alpha}$, $EW_{[O\,III]}$ and $\Delta v_{Ly\alpha}$. We suggest the reason for this dichotomy could owe to three factors: anisotropic escape where LyC photons escape through channels and the opening angle of these channels is only aligned with our line of sight for the detections, a time varying f_{esc} due to the bursty nature of star-formation in these low-mass systems, or spatially varying H I in the IGM of the SSA22 protocluster which appears to have a higher H I density compared to similar control fields (Mawatari et al. 2017).

The large f_{esc} detected by the LACES program, the fraction of LAEs which leak LyC photons, and the large difference in Lyman continuum flux between detected and non-detected objects may hold significant implications for understanding the mechanisms through which hydrogen ionizing radiation escapes from galaxies. Coupled with our observations that suggest faint, low-mass LAEs with strong Lyα and large $EW_{[O\,III]}$ have the most extreme f_{esc}, our results provide exciting hints for how to answer the question of whether galaxies served as the primary driver of cosmic reionization.

We acknowledge financial support from European Research Council Advanced Grant FP7/669253 (TF, RSE). BER is partially supported by NASA program HST-GO-14747, contract NNG16PJ25C, and grant 17-ATP17-0034. KN acknowledges a JSPS Overseas Research Fellowship and a JSPS Research Fellowship for Young Scientists. DPS acknowledges support from the National Science Foundation through grant AST-1410155. AKI is supported by the Japan Society for the Promotion of Science, KAKENHI Grant Number 17H01114. This work is based on observations taken by the NASA/ESA HST, which is operated by the Association of Universities for Research in Astronomy, Inc., under NASA contract NAS5-26555. We thank Masato Onodera for observing 1 of our 4 MOSFIRE K band masks. We also thank T. Hayashino, T. Yamada and Y. Matsuda for providing the LAE catalogue and the ground-based photometric data. We would also like to thank K. Kakiichi and N. Laporte for useful comments. Further data was taken with the Subaru telescope and the W.M. Keck Observatory on Maunakea, Hawaii the latter of which is operated as a scientific partnership among the California Institute of Technology, the University of California and the National Aeronautics and Space Administration. This Observatory was made possible by the generous financial support of the W. M. Keck Foundation. The authors wish to recognize and acknowledge the very significant cultural role and reverence that the summit of Maunakea has always had within the indigenous Hawaiian community. We are most fortunate to have the opportunity to conduct observations from this mountain.

REFERENCES

Atek, H., Richard, J., Kneib, J.-P., et al. 2015, ApJ, 800, 18
Barbary, K. 2016, The Journal of Open Source Software, 2016
Beckwith, S. V. W., Stiavelli, M., Koekemoer, A. M., et al. 2006, AJ, 132, 1729
Behrens, C., Dijkstra, M., & Niemeyer, J. C. 2014, A&A, 563, A77
Bertin, E. 2010, Astrophysics Source Code Library
Bertin, E., & Arnouts, S. 1996, A&AS, 117, 393
Bian, F., Fan, X., McGreer, I., Cai, Z., & Jiang, L. 2017, ApJ, 837, L12
Bouwens, R. J., Smit, R., Labbé, I., et al. 2016, ApJ, 831, 176
Bouwens, R. J., Illingworth, G. D., Oesch, P. A., et al. 2012, ApJ, 752, L5
—. 2015, ApJ, 803, 34
Bradley, L. D., Zitrin, A., Coe, D., et al. 2014, ApJ, 792, 76
Calzetti, D., Kinney, A. L., & Storchi-Bergmann, T. 1994, ApJ, 429, 582
de Barros, S., Vanzella, E., Amorín, R., et al. 2016, A&A, 585, A51
Dijkstra, M., Gronke, M., & Venkatesan, A. 2016, ApJ, 828, 71
Eldridge, J., Stanway, E., Xiao, L., et al. 2017, Publications of the Astronomical Society of Australia, 34
Eldridge, J. J., & Stanway, E. R. 2009, MNRAS, 400, 1019
—. 2012, MNRAS, 419, 479
Ellis, R. S., McLure, R. J., Dunlop, J. S., et al. 2013, ApJ, 763, L7
Faisst, A. L. 2016, ApJ, 829, 99
Feroz, F., & Hobson, M. P. 2008, MNRAS, 384, 449
Feroz, F., Hobson, M. P., & Bridges, M. 2009, MNRAS, 398, 1601
Finkelstein, S. L., Papovich, C., Ryan, R. E., et al. 2012, ApJ, 758, 93
Finkelstein, S. L., Ryan, Jr., R. E., Papovich, C., et al. 2015, ApJ, 810, 71
Fontanot, F., Cristiani, S., Pfrommer, C., Cupani, G., & Vanzella, E. 2014, MNRAS, 438, 2097
Fontanot, F., Cristiani, S., & Vanzella, E. 2012, MNRAS, 425, 1413
Gordon, K. D., Clayton, G. C., Misselt, K. A., Landolt, A. U., & Wolff, M. J. 2003, ApJ, 594, 279
Grazian, A., Giallongo, E., Paris, D., et al. 2017, A&A, 602, A18
Grogin, N. A., Kocevski, D. D., Faber, S. M., et al. 2011, ApJS, 197, 35
Hayashino, T., Matsuda, Y., Tamura, H., et al. 2004, AJ, 128, 2073
Hayashino, T., et al. 2018, MNRAS, submitted
Hayes, M. 2015, Publications of the Astronomical Society of Australia, 32, e027
Illingworth, G. D., Magee, D., Oesch, P. A., et al. 2013, ApJS, 209, 6
Inoue, A. K., & Iwata, I. 2008, MNRAS, 387, 1681
Inoue, A. K., Iwata, I., & Deharveng, J.-M. 2006, MNRAS, 371, L1
Inoue, A. K., Iwata, I., Deharveng, J.-M., Buat, V., & Burgarella, D. 2005, A&A, 435, 471
Inoue, A. K., Shimizu, I., Iwata, I., & Tanaka, M. 2014, MNRAS, 442, 1805
Inoue, A. K., Kousai, K., Iwata, I., et al. 2011, MNRAS, 411, 2336
Ishigaki, M., Kawamata, R., Ouchi, M., et al. 2018, ApJ, 854, 73
Iwata, I., Inoue, A. K., Matsuda, Y., et al. 2009, ApJ, 692, 1287
Izotov, Y. I., Orlitová, I., Schaerer, D., et al. 2016a, Nature, 529, 178
Izotov, Y. I., Schaerer, D., Thuan, T. X., et al. 2016b, MNRAS, 461, 3683
Izotov, Y. I., Schaerer, D., Worseck, G., et al. 2018, MNRAS, 474, 4514
Japelj, J., Vanzella, E., Fontanot, F., et al. 2017, MNRAS, 468, 389
Jaskot, A. E., & Oey, M. S. 2013, ApJ, 766, 91
Kimm, T., & Cen, R. 2013, ApJ, 776, 35
Kimm, T., Katz, H., Haehnelt, M., et al. 2017, MNRAS, 466, 4826
Koekemoer, A. M., Faber, S. M., Ferguson, H. C., et al. 2011, ApJS, 197, 36

Koekemoer, A. M., Ellis, R. S., McLure, R. J., et al. 2013, ApJS, 209, 3
Kuhlen, M., & Faucher-Giguère, C.-A. 2012, MNRAS, 423, 862
Labbé, I., Oesch, P. A., Bouwens, R. J., et al. 2013, ApJ, 777, L19
Laporte, N., Nakajima, K., Ellis, R. S., et al. 2017, ApJ, 851, 40
Livermore, R. C., Finkelstein, S. L., & Lotz, J. M. 2017, ApJ, 835, 113
Lotz, J. M., Koekemoer, A., Coe, D., et al. 2017, ApJ, 837, 97
Ma, X., Hopkins, P. F., Kasen, D., et al. 2016, MNRAS, 459, 3614
Madau, P. 1995, ApJ, 441, 18
Madau, P., & Haardt, F. 2015, ApJ, 813, L8
Mainali, R., Zitrin, A., Stark, D. P., et al. 2018, ArXiv e-prints, arXiv:1804.00041
Marchi, F., Pentericci, L., Guaita, L., et al. 2017, ArXiv e-prints, arXiv:1710.10184
Matsuda, Y., Yamada, T., Hayashino, T., Yamauchi, R., & Nakamura, Y. 2006, ApJ, 640, L123
Matsuda, Y., Yamada, T., Hayashino, T., et al. 2005, ApJ, 634, L125
Matthee, J., Sobral, D., Best, P., et al. 2017, MNRAS, 465, 3637
Mawatari, K., Inoue, A. K., Yamada, T., et al. 2017, MNRAS, 467, 3951
McLeod, D. J., McLure, R. J., Dunlop, J. S., et al. 2015, MNRAS, 450, 3032
McLure, R. J., Dunlop, J. S., Bowler, R. A. A., et al. 2013, MNRAS, 432, 2696
Merlin, E., Fontana, A., Ferguson, H. C., et al. 2015, A&A, 582, A15
Merlin, E., Bourne, N., Castellano, M., et al. 2016, A&A, 595, A97
Micheva, G., Iwata, I., & Inoue, A. K. 2017a, MNRAS, 465, 302
Micheva, G., Iwata, I., Inoue, A. K., et al. 2017b, MNRAS, 465, 316
Mostardi, R. E., Shapley, A. E., Nestor, D. B., et al. 2013, ApJ, 779, 65
Mostardi, R. E., Shapley, A. E., Steidel, C. C., et al. 2015, ApJ, 810, 107
Naidu, R. P., Forrest, B., Oesch, P. A., Tran, K.-V. H., & Holden, B. P. 2018, MNRAS, arXiv:1804.06845
Nakajima, K., Ellis, R. S., Iwata, I., et al. 2016, ApJ, 831, L9
Nakajima, K., Fletcher, T., Ellis, R. S., Robertson, B. E., & Iwata, I. 2018, ArXiv e-prints, arXiv:1801.03085
Nakajima, K., & Ouchi, M. 2014, MNRAS, 442, 900
Nestor, D. B., Shapley, A. E., Kornei, K. A., Steidel, C. C., & Siana, B. 2013, ApJ, 765, 47
Nestor, D. B., Shapley, A. E., Steidel, C. C., & Siana, B. 2011, ApJ, 736, 18
Nonino, M., Dickinson, M., Rosati, P., et al. 2009, ApJS, 183, 244
Oesch, P. A., Bouwens, R. J., Illingworth, G. D., et al. 2013, ApJ, 773, 75
Oesch, P. A., van Dokkum, P. G., Illingworth, G. D., et al. 2015, ApJ, 804, L30
Oke, J. B., & Gunn, J. E. 1983, ApJ, 266, 713
Ono, Y., Ouchi, M., Shimasaku, K., et al. 2010, MNRAS, 402, 1580
Ono, Y., Ouchi, M., Mobasher, B., et al. 2012, ApJ, 744, 83
Paardekooper, J.-P., Khochfar, S., & Dalla Vecchia, C. 2015, MNRAS, 451, 2544
Papovich, C., Dickinson, M., & Ferguson, H. C. 2001, ApJ, 559, 620
Roberts-Borsani, G. W., Bouwens, R. J., Oesch, P. A., et al. 2016, ApJ, 823, 143
Robertson, B. E., Ellis, R. S., Dunlop, J. S., McLure, R. J., & Stark, D. P. 2010, Nature, 468, 49
Robertson, B. E., Ellis, R. S., Furlanetto, S. R., & Dunlop, J. S. 2015, ApJ, 802, L19
Robertson, B. E., Furlanetto, S. R., Schneider, E., et al. 2013, ApJ, 768, 71
Rutkowski, M. J., Scarlata, C., Henry, A., et al. 2017, ApJ, 841, L27
Schenker, M. A., Ellis, R. S., Konidaris, N. P., & Stark, D. P. 2013, ApJ, 777, 67
Schenker, M. A., Stark, D. P., Ellis, R. S., et al. 2012, ApJ, 744, 179
Shapley, A. E., Steidel, C. C., Pettini, M., Adelberger, K. L., & Erb, D. K. 2006, ApJ, 651, 688
Shapley, A. E., Steidel, C. C., Strom, A. L., et al. 2016, ApJ, 826, L24
Shivaei, I., Reddy, N. A., Siana, B., et al. 2018, ApJ, 855, 42
Siana, B., Shapley, A. E., Kulas, K. R., et al. 2015, ApJ, 804, 17
Smit, R., Bouwens, R. J., Labbé, I., et al. 2014, ApJ, 784, 58
Smit, R., Bouwens, R. J., Franx, M., et al. 2015, ApJ, 801, 122
Stanway, E. R., Eldridge, J. J., & Becker, G. D. 2016, MNRAS, 456, 485
Stark, D. P. 2016, ARA&A, 54, 761
Stark, D. P., Ellis, R. S., Chiu, K., Ouchi, M., & Bunker, A. 2010, MNRAS, 408, 1628
Stark, D. P., Walth, G., Charlot, S., et al. 2015, MNRAS, 454, 1393
Stark, D. P., Ellis, R. S., Charlot, S., et al. 2017, MNRAS, 464, 469
Steidel, C. C., Bogosavlevic, M., Shapley, A. E., et al. 2018, ArXiv e-prints, arXiv:1805.06071
Steidel, C. C., Pettini, M., & Adelberger, K. L. 2001, ApJ, 546, 665
Tang, M., et al. 2018, in prep.
Trebitsch, M., Blaizot, J., Rosdahl, J., Devriendt, J., & Slyz, A. 2017, MNRAS, 470, 224
Vanzella, E., Siana, B., Cristiani, S., & Nonino, M. 2010, MNRAS, 404, 1672
Vanzella, E., de Barros, S., Vasei, K., et al. 2016, ApJ, 825, 41
Vanzella, E., Nonino, M., Cupani, G., et al. 2018, MNRAS, 476, L15
Verhamme, A., Orlitová, I., Schaerer, D., & Hayes, M. 2015, A&A, 578, A7
Verhamme, A., Orlitová, I., Schaerer, D., et al. 2017, A&A, 597, A13
Wise, J. H., Demchenko, V. G., Halicek, M. T., et al. 2014, MNRAS, 442, 2560
Yamada, T., Matsuda, Y., Kousai, K., et al. 2012a, ApJ, 751, 29
Yamada, T., Nakamura, Y., Matsuda, Y., et al. 2012b, AJ, 143, 79
Zackrisson, E., Inoue, A. K., & Jensen, H. 2013, ApJ, 777, 39
Zitrin, A., Labbé, I., Belli, S., et al. 2015, ApJ, 810, L12